Journal of African Earth Sciences 100 (2014) 656–674

Contents lists available at ScienceDirect

Journal of African Earth Sciences

journal homepage: www.elsevier.com/locate/jafrearsci

Petrography, geochemistry and U–Pb zircon age of the Matongo carbonatite Massif (Burundi): Implication for the Neoproterozoic geodynamic evolution of Central Africa

Gilbert Midende [a], Philippe Boulvais [b], Luc Tack [c], Frank Melcher [d], Axel Gerdes [e], Stijn Dewaele [c], Daniel Demaiffe [f], Sophie Decrée [c,g,*]

[a] Université du Burundi, Bujumbura, Burundi
[b] Géosciences Rennes, UMR 6118, Université de Rennes 1, France
[c] Royal Museum for Central Africa, Tervuren, Belgium
[d] Chair of Geology and Economic Geology, University of Leoben, Austria
[e] Geozentrum der Goethe-Universität, Institut für Geowissenschaften, Frankfurt am Main, Germany
[f] Université Libre de Bruxelles, DSTE, CP160/02, Belgium
[g] Royal Belgian Institute of Natural Sciences, Brussels, Belgium

ARTICLE INFO

Article history:
Received 6 February 2014
Received in revised form 20 August 2014
Accepted 21 August 2014
Available online 2 September 2014

Keywords:
Matongo
Upper Ruvubu
Carbonatite
Alkaline magmatism
Neoproterozoic
Burundi

ABSTRACT

The Matongo carbonatite intrusion belongs to the Neoproterozoic Upper Ruvubu alkaline plutonic complex (URAPC), that is located in Burundi along the western branch of the East African Rift. Beside the Matongo carbonatite, the URAPC alkaline complex comprises feldspathoidal syenites, diorites, quartz-bearing syenites and granites.

Three main facies have been recognized in the Matongo carbonatite: (1) Sövites represent the dominant facies. Two varieties have been recognized. A scarce coarse-grained sövite (sövite I), which is altered and poorly enriched in REE ($4 < \Sigma REE < 8$ ppm), is encountered in highly fractured zones. A fine-grained sövite (sövite II), which is made of saccharoidal calcite, commonly associated with apatite, aegirine and amphibole, is abundant in the intrusion. Sövite II is enriched in LREE ($442 < \Sigma REE < 1550$ ppm, $49 < La_N/Yb_N < 175$). (2) Ferrocarbonatites, that form decimeter-wide veins crosscutting the sövites, are characterized by a LREE enriched patterns ($225 < \Sigma REE < 1048$ ppm, $17 < La_N/Yb_N < 64$). (3) K-feldspar and biotite-rich fenite facies (silicocarbonatites) have been recognized at the contact between the carbonatites and the country rock. They are likewise LREE-enriched ($134 < \Sigma REE < 681$ ppm, $25 < La_N/Yb_N < 46$). Additionaly, "late" hydrothermal MREE-rich carbonatite veinlets can be found in sövite I. They are characterized by moderate enrichment in REE ($\Sigma REE = 397$ ppm), with a MREE-humped pattern ($La_N/Yb_N = 3.7$). The different facies represent the typical magmatic evolution of a carbonatite, while the silicocarbonatites are interpreted as resulting from the fenitisation of the country host-rocks. In addition, the most REE-depleted and fractionated facies, i.e. the coarse-grained sövite facies and the "late" calcite veinlets testify for hydrothermal processes that occurred after carbonatite emplacement and result from REE mobilization and redistribution.

Large idiomorphic zircon crystals (megacrysts), found in the vicinity of the carbonatite can directly be related to the carbonatite evolution. They have been dated at 705.5 ± 4.5 Ma (U–Pb concordant age, LA–ICP–MS). Similar zircon megacrysts of the Lueshe carbonatite (DRCongo) have been dated and give a concordant age at 798.5 ± 4.9 Ma (U–Pb, LA–ICP–MS). Considering that an extensional tectonic regime occured at that time in Central Africa – what remains debated - both ages could relate to different stages of Rodinia breakup, with uprise of mantle-derived magmas along Palaeoproterozoic lithospheric zones of weakness.

* Corresponding author at: Royal Belgian Institute of Natural Sciences, Brussels, Belgium.
E-mail addresses: midendegilbert@yahoo.com (G. Midende), philippe.boulvais@univ-rennes1.fr (P. Boulvais), luc.tack@africamuseum.be (L. Tack), frank.melcher@unileoben.ac.at (F. Melcher), gerdes@em.uni-frankfurt.de (A. Gerdes), stijn.dewaele@africamuseum.be (S. Dewaele), ddemaif@ulb.ac.be (D. Demaiffe), sophie.decree@naturalsciences.be (S. Decrée).

http://dx.doi.org/10.1016/j.jafrearsci.2014.08.010
1464-343X/

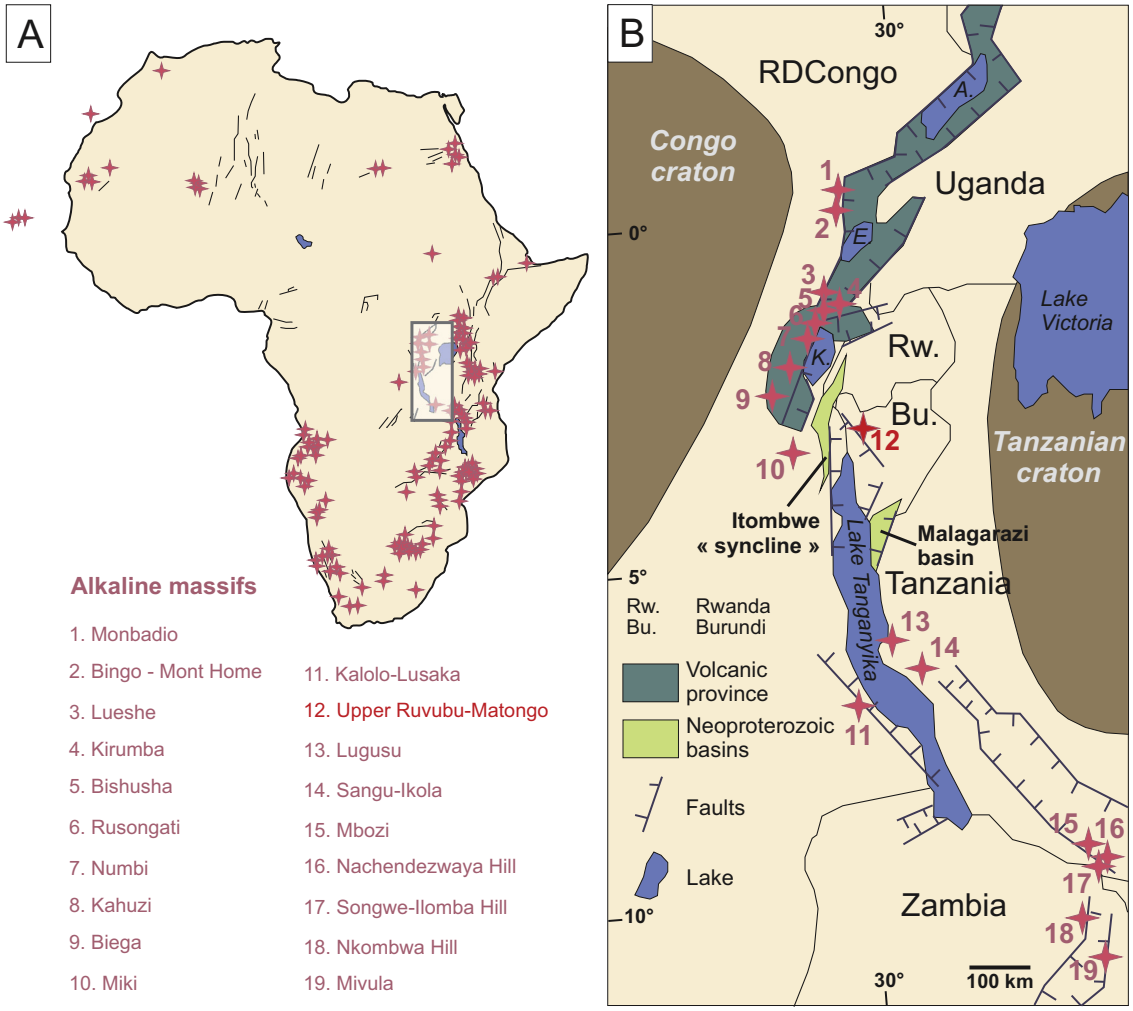

Fig. 1. (A) Carbonatite and alkaline massif occurrences in Africa (redrawn from Woolley, 2001), (B) Alkaline magmatism along the western branch of the East African Rift system (redrawn from Tack et al., 1984 and Kampunzu and Mohr, 1991). The Itombwe "syncline" and Malagarazi basin consist of Neoproterozoic rocks; the Malagarazi Supergroup (Burundi) – formerly known in Tanzania as Bukoba Supergroup – has been renamed Nyamuri Supergfroup (Geology and Mineral map of Tanzania, 1:2.000.000, 2008). (For interpretation of the references to colour in this figure legend, the reader is referred to the web version of this article.)

1. Introduction

More than 850 alkaline complexes and carbonatites have been recognized in Africa (Woolley, 2001; Fig. 1A). They represent about 40% of the world known occurrences. Their ages range from 2 Ga (Phalaborwa, South Africa) to the present (Oldoinyo Lengai, Tanzania), with two abundance peaks during the Lower Paleozoic and the Cretaceous. Half of the African carbonatites are spatially associated to the African rift (Woolley, 2001). In central Africa, Tack et al. (1984) and Kampunzu et al. (1985) have recognized 23 Neoproterozoic alkaline plutonic massifs that are distributed over a distance of 1700 km along the present-day Western Rift (i.e. the western branch of the East African Rift) (Fig. 1B).

Among these massifs, the Matongo carbonatite in Burundi is part of the Neoproterozoic Upper Ruvubu Alkaline Plutonic Complex (URAPC, Fig. 2). This carbonatite does not outcrop and was discovered by drilling in the 80s. It displays a classical magmatic series, with a calciocarbonatite-ferrocarbonatite-fenite suite (Midende, 1984), and shows exceptional mineralization features, including large (>1 cm) zircons (Burke, 1998; Fransolet and Tack, 1992).

The Matongo carbonatite occurs in the central part of the URAPC, which consists of an outer unit of quartz-bearing syenite, granite and gabbro-diorite and an inner unit, characterized by the presence of feldspathoidal syenite and monzonite. The whole complex was dated between ~760 and ~690 Ma (Demaiffe, 2008; Tack et al., 1984; Van den Haute, 1986). Its emplacement has been related to a linear intraplate reactivation event (Tack et al., 1996), which marked the breakup of the Rodinia Supercontinent (Kampunzu et al., 1997). The relationship with Rodinia breakup has already been evoked for other Neoproterozoic alkaline massifs in the area, e.g. for the Lueshe complex in RDC (Kampunzu et al., 1998; Kramm et al., 1997; Maravic and Morteani, 1980; Maravic et al., 1989; Van Overbeke et al., 1996).

This study represents a comprehensive petrographical and geochemical study of the Matongo carbonatite (the petrological evolution of the complex is however beyond the scope of the study), together with new LA–ICP–MS U–Th–Pb ages obtained on its zircon megacrysts. For comparison, zircon megacrysts from the Lueshe carbonatite have also been dated. This study is envisaged to describe the (post-)magmatic processes associated with the carbonatite emplacement and to position the Matongo carbonatitic event in the Neoproterozoic geodynamic context of Central Africa (Neoproterozoic supercontinent fragmentation/amalgamation).

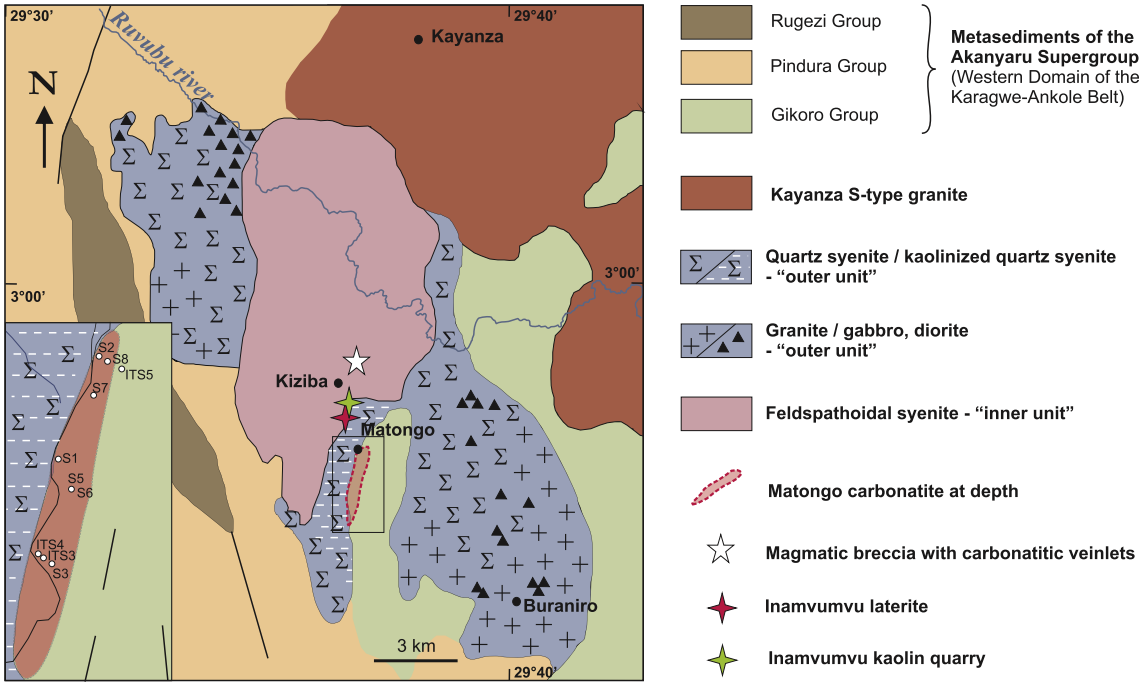

Fig. 2. Geological sketch map of the studied area (modified and redrawn from Tack et al., 1984, and after Fernandez-Alonso et al., 2012), with location of the showings/deposits mentioned in the text. The insert illustrates the location of the drill holes.

2. Geological setting

The Matongo carbonatite belongs to the Neoproterozoic Upper Ruvubu Alkaline Plutonic Complex (URAPC), located in the western part of Burundi along the western branch of the East African Rift (Tack et al., 1984). The complex is hosted in rocks belonging to the Mesoproterozoic Karagwe–Ankole Belt (KAB; Fernandez-Alonso et al., 2012), which consists of metasedimentary (phyllites, graphitic schists, metaquartzites and dolomite lenses and interbedded metavolcanic rocks of Palaeo- or Mesoproterozoic age (Cahen et al., 1984; Brinckmann et al., 2001; Fernandez-Alonso et al., 2012). The metasedimentary and metavolcanic rocks of the Western Domain (WD) of the KAB were intruded by S-type granites, which are part of the 1375 Ma old bimodal magmatic "Kibaran event" (U–Pb SHRIMP on zircon; Tack et al., 2010). At 986 ± 10 Ma (U–Pb SHRIMP on zircon; Tack et al., 2010) "Tin granites" were emplaced. The magmatism has been related to the ~1.0 Ga Southern Irumides collisional orogeny, corresponding to the Rodinia amalgamation (Fernandez-Alonso et al., 2012). The orogeny is responsible for the general fold-and-thrust-belt geometry of the KAB (Fernandez-Alonso et al., 2012). The tin mineralisation was emplaced in a relaxational setting following the deformation (Dewaele et al., 2011; Melcher et al., 2013). In the URAPC region, pegmatites including feldspar, quartz, muscovite, biotite and more exceptionally black tourmaline, cassiterite and garnet have been dated between 977 ± 8 Ma (Rb–Sr on muscovite and feldspar; Cahen and Ledent, 1979) and 969 ± 8 Ma (Rb–Sr on muscovite and whole-rock; Brinckmann and Lehmann, 1983).

Later events in the KAB have been related to Panafrican tectonothermal processes in the Western Rift area as (1) brittle reworking of pegmatites along fractures at 628 ± 110 Ma and 622 ± 56 Ma (Romer and Lehmann, 1995), (2) muscovite Ar–Ar resetting ages in Rwanda (Sn–Ta pegmatite at 593 Ma; Dewaele et al., 2011), and (3) N–S trending shear-controlled gold mineralization emplacement at 535 in NW Burundi (Brinckmann et al., 2001). Such Panafrican overprint has not been recognized in the URAPC area yet. At ~750 Ma, in probable association with the Rodinia Supercontinent breakup (Kampunzu et al., 1997), some 23 alkaline complexes were emplaced along lithosphere-scale shear zones (Tack et al., 1996). The URAPC, roughly NW–SE oriented, is made up of both a silica-oversaturated and silica-undersaturated unit as well as a carbonatite (the Matongo carbonatite; Fig. 2). The "outer unit" comprises an intimate association of plutonic rocks from olivine-bearing gabbros and diorites, to granites and quartz-bearing syenites. The "inner unit" comprises feldspathoidal syenites and monzonites. Numerous dykes of feldspathoidal syenite intrude the "outer unit", especially in its western part (Buysschaert, 1993; Tack et al., 1984; Vergauwen, 1990). The whole complex has undergone extensive supergene lateritization. Kaolinitization, notably in the region close to Matongo where kaolinite has been exploited (Inamvumvu), is developed on top of the subsurface carbonatite in a contact aureole as a result of hydrothermal alteration of the host quartz-bearing syenites.

The Matongo carbonatite is only known by drilling in the Matongo area (Fig. 2). It occurs at a depth of about 40–80 m and forms a NNE elongated intrusion of 2750 m long and 250 m wide. Interstingly, another hidden carbonatitic body is inferred in Burundi (Van Wambeke, 1977), in the Gakara–Karonge area (60 km far from Matongo), which is known for its REE hydrothermal deposits (Lehmann et al., 1994).

Fine- and coarse-grained calciocarbonatite and a ferrocarbonatite have been identified in the Matongo carbonatite (Demaiffe, 2008; Midende, 1984). "Late" calcite veinlets that crosscut the coarse-grained calciocarbonatite have been interpreted to represent a hydrothermal event (Midende, 1984). Fenitization is also well developed in the external part of the carbonatite (Midende, 1984). The Sr and Nd isotope compositions indicate a cogenetic relation between the carbonatite and felspathoidal syenites (Tack et al., 1996). Initial εNd values (+0.7 to +5.2) and low initial $^{86}Sr/^{87}Sr$ ratios of 0.7025–0.7030 support a mantle-derived origin for the URAPC rocks without evidence for significant assimilation of crustal material (Tack et al., 1984). The inferred source appears less depleted in incompatible elements than the typical Depleted Mantle (DM) (Demaiffe, 2008).

Available ages on the URAPC show some inconsistency. For the "outer unit" U–Pb on zircon fraction and zircon Pb-evaporation ages at 748 ± 2 Ma and 741 ± 2 Ma respectively (Tack et al., 1995) have been obtained, while a Rb–Sr whole rock isochron yielded an age of 707 ± 17 Ma (Tack et al., 1984). U–Pb on bulk zircon on the "inner unit" of the URAPC gave an age of 739 ± 7 Ma, while the Rb–Sr isochron age of this unit yielded an age of 699 ± 13 Ma (Tack et al., 1984). Also, a fission track age on sphene of 762 ± 33 Ma has been obtained on the "inner unit" (Van den Haute, 1986) and is questionnable as being older than U–Pb zircon age. On the Matongo carbonatite, a Pb–Pb isochron age of 690 ± 32 Ma (Demaiffe, 2008) is consistent with the Rb–Sr age (699 Ma) but significantly younger than the U–Pb zircon age (739 Ma) of the "inner unit". Concerning the zircon megacrysts, lead-evaporation ages of yielded an age of 738 ± 4 Ma (Tack et al., 1995). For the Lueshe Complex, the geochronological data are Rb-Sr isochron ages on whole rocks, varying between 548–568 Ma (Kramm et al., 1997), 619 ± 42 Ma (Van Overbeke, 1996) and 822 ± 120 Ma (Kampunzu et al., 1998), and a K-Ar biotite age (516 ± 26 Ma; Bellon and Pouclet, 1980). These ages overlap the URAPC zircon existing ages.

3. Zircon megacrysts from Matongo (Burundi) and Lueshe (DRC)

Near Matongo, numerous idiomorphic zircon megacrysts, up to 6 cm in size, in association with ilmenite megacrysts, are disseminated in a dismembered lateritic crust and in the kaolin of the Inamvumvu hill (Fig. 2). Trenching during carbonatite exploration works in the 80s (British Sulphur Company, unpublished internal report), exposed zircon megacrysts in "pegmatitic-like" veinlets intruding supergene weathered rock with preserved original coarse-grained magmatic texture (quartz-bearing syenite or granite) (Tack, unpublished data). No more outcrop still exists. At Kiziba (Fig. 2), a comparable, although smaller (up to 1 cm in size) zircon megacrysts occur in coarse-grained veins within the feldspathoidal syenite (Fransolet and Tack, 1992), in association with alkali feldspar, nepheline, sodalite, fluorite, biotite, aegirine, calcite and ilmenite.

The zircon megacrysts of the Inamvumvu hill, from where our samples come from, are characterized by Th- and U-rich homogeneous cores and partially metamict, oscillatory zoned outer rims (Burke, 1998). They contain ubiquitous primary carbonate inclusions (calcite, magnesian calcite and nahcolite; Burke, 1998) and are thought to have crystallized from the circulation of alkaline fluids associated with the carbonatite-feldspathoidal syenite emplacement (Fransolet and Tack, 1992), i.e. relatively late in the frame of the URAPC emplacement.

Similar zircon megacrysts around 2 cm in size are also known from the Lueshe complex (Fig. 1B), in particular in the silico-sövite parent rock predating the Lueshe carbonatite (Maravic, 1983; Maravic and Morteani, 1980; Philippo, 1995), i.e. relatively early in the frame of the Lueshe emplacement. Isolated zircon megacrysts are also found in the lateritic crust, in association with pyrochlore, ilmenorutile and primary or secondary phosphates. Idiomorphic and well-preserved megacrysts occur in the small Lueshe river (sample RGM 9673, 5–6 mm wide, is one of these). These zircon grains likely derive from the the silico-sövite upstream, with almost no transport.

4. Sampling and analytical techniques

Twenty-one samples of the Matongo carbonatite have been studied. The samples originate from 10 drill cores (from 56 to 291 m depth), from a drilling program performed in 1976–1978 by the United Nations Development Program (location of the boreholes on Fig. 2). Other samples studied are surface samples from the rock collection of the Royal Museum for Central Africa (RMCA), Tervuren (Belgium).

Petrographic description was carried out by polarized light microscopy on thin sections. Mineral compositions were measured by electron microprobe analysis (EPMA) at the Université de Louvain (UCL, Belgium). Chemical compositions of rock samples were obtained on finely grained powders (about 100 g) by X-ray fluorescence (XRF) at the University of Brussels (ULB, Belgium) for major elements analyses and at Liège (ULg, Belgium) for major and trace elements (Rb, Sr, Ba, V and Nb). Other trace element compositions have been determined at the Katholieke Universiteit Leuven (KULeuven, Belgium) by neutron activation analyses (Midende, 1984). Additional chemical analyses were performed by the Actlabs laboratory (Ontario, Canada) using ICP-AES and ICP-MS methods for major and trace elements respectively.

The dated zircon megacrysts were mounted in epoxy resin, cut and polished (BGR, Hanover, Germany). Characterization of internal textures was accomplished using back-scattered electrons (BSE) and cathodoluminescence (CL) images generated on a CAMECA SX100 electron microprobe at the BGR. Furthermore, zircons were quantitatively analyzed using wavelength-dispersive spectrometry on the same instrument using 15 kV acceleration voltage and 40 nA sample current. The following elements were measured (line, spectrometer, standard, measurement time on peak): SiKα (TAP, zircon, 10); ZrLα (PET, zircon, 10); HfMα (TAP, hafnon, 90); AlKα (TAP, metal, 20); FeKα (LLIF, metal, 60); MnKα (LLIF, metal, 60); PKα (LPET, apatite, 20); CaKα (LPET, apatite, 10); TiKα (LPET, metal, 20); PbMα (LPET, galena, 90); ThMα (PET, metal, 110); UMα (LPET, metal, 100).

Uranium, thorium and lead isotope analyzes were carried out by LA–ICP–MS at the Goethe University of Frankfurt (Germany), using a slightly modified method, as previously described in Gerdes and Zeh (2006, 2009) and Zeh and Gerdes (2012). A ThermoScientific Element 2 sector-field ICP-MS was coupled to a Resolution M-50 (Resonetics) 193 nm ArF Excimer laser (CompexPro 102, Coherent) equipped with a two-volume ablation cell (Laurin Technic, Australia). The laser was fired with 5.5 Hz at a fluence of about 3–4 J cm^{-2}. Raw data were corrected offline for background signal, common Pb, laser induced elemental fractionation, instrumental mass discrimination and time-dependent elemental fractionation of Pb/U using an in-house MS Excel© spreadsheet program (Gerdes and Zeh, 2006, 2009). Laser-induced elemental fractionation and instrumental mass discrimination were corrected by normalization to the reference zircon GJ-1 (0.0984 ± 0.0003; ID-TIMS GUF value).

5. Petrography and mineralogy of the Matongo carbonatite

Midende (1984) provided detailed descriptions of the different rocks of the Matongo carbonatite, which are complemented by our observations and new data on mineral composition (see Supplementary data).

5.1. Magmatic facies

The carbonatite comprises three main magmatic facies (Demaiffe, 2008; Midende, 1984).

The sövite I facies is limited and localized in highly fractured zones of the carbonatite. Calcite grains are euhedral, up to 2 cm in size (Fig. 3A), and close to pure calcite in composition (CaO close to 55 wt.%), with minor contribution of Mn and Mg (Table 1). At the contact with the host rocks, sövite I can be silicified, Fe-stained and/or crosscut by fissures filled with iron oxides and quartz.

The sövite II represents the dominant facies of the carbonatite. It mainly consists of saccharoidal calcite (polygonal mosaic), with

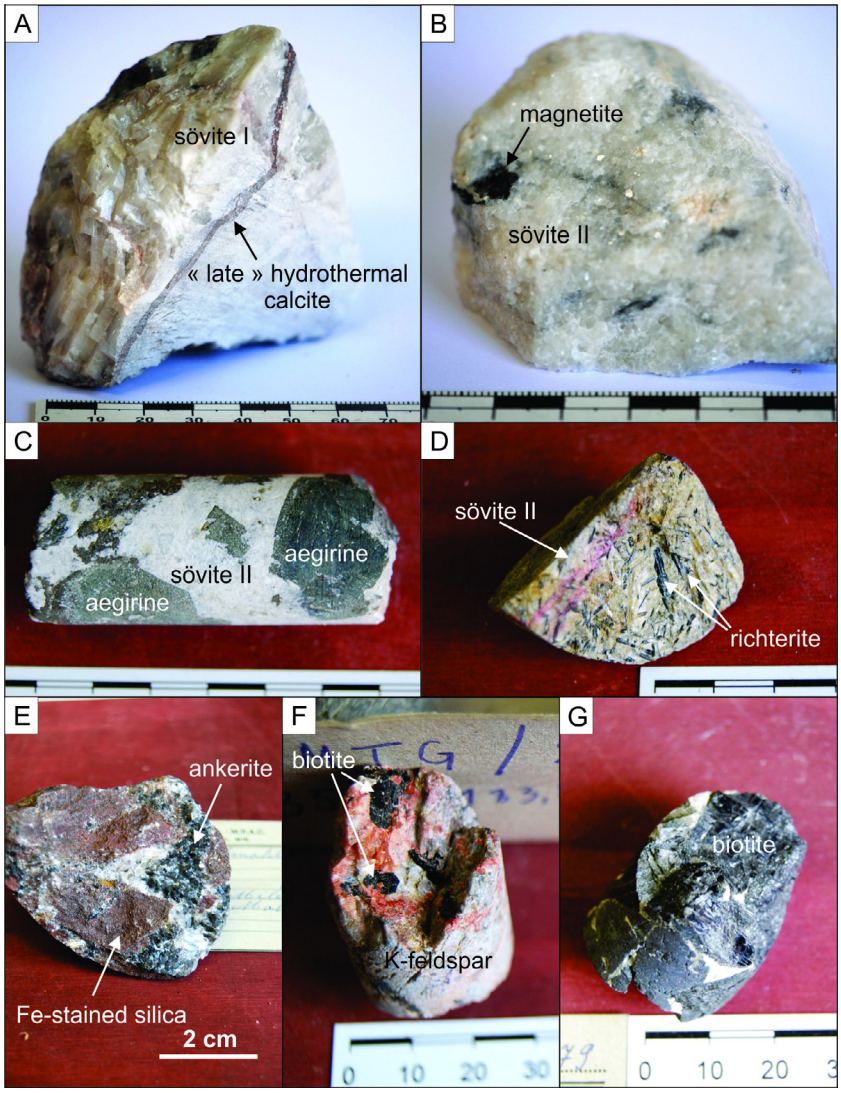

Fig. 3. Photomacrographs of the various Matongo carbonatite facies: (A) coarse-grained sövite I, cut by a vein of "late" hydrothermal calcite (calcite finely admixed with Fe oxides) (sample LT-SI-1), (B) fine-grained sövite II with biotite (sample LT-SII-1), (C) euhedral crystals of aegirine in a sövite II (sample RG 140.280A), (D) richterite needles within a sövite II (sample RG 140.280B), (E) association of ankerite (dark grey on the picture), calcite and iron-stained silica (red on the picture) (sample RG 140.272), (F) fenite comprizing K-feldspar and biotite (sample S1/183.5–184.25) and (G) fenite almost exclusively made up of biotite (sample RG 140.279). Scale bars are in cm. (For interpretation of the references to color in this figure legend, the reader is referred to the web version of this article.)

grain sizes ranging from 1 to 4 mm in width (Fig. 3B). The calcite contains Fe (FeO between 0.5 and 3 wt.%), Mg (MgO between 0.1 and 1.6 wt.%) and Sr (SrO between 0.8 and 1.5 wt.%). Sövite II commonly contains discrete zones with vanadiferous aegirine (1.1–1.9 wt.% V_2O_3), occurring as euhedral elongated crystals up to 2 cm in length (Fig. 3C), and apatite occurring as small grains or small prismatic crystals up to 5 mm in size. Aegirine and apatite may represent local cumulates, in which pyrochlore ($(Na,Ca)_2Nb_2O_6(OH,F)$) and K-feldspar are also present. The vanadiferous aegirine is partly transformed into amphibole (Mg-arfvedsonite; see Supplementary data), which developed along aegirine cleavages and/or crystal boundaries. Richterite, another alkali amphibole, with 8.1–12.4 wt.% Fe_2O_3, 3.2–5.8 wt.% FeO, 14.2–16.6 wt.% MgO, 4.2–6 wt.% CaO, 3.6–5.1 wt.% Na_2O and 0.6–2.0 wt.% K_2O, occurs as cm-long needles (Fig. 3D) and may constitute 30% of the sövite rock volume. It is associated with calcite, apatite, clinopyroxene and phlogopite (See Supplementary data).

The ferrocarbonatite facies forms decimeter-wide veins crosscutting the sövites. It consists of fine-grained (<1 mm in width) dolomite and ankerite (13.7–15.4 wt.% FeO, 11.3–13.7 wt.% MgO, 0.3–0.7 wt.% MnO; Fig. 3E), with abundant euhedral V-rich magnetite (V_2O_3, up to 2 wt.%) and ilmenite crystals. Iron-stained silica veins locally crosscut this facies (Fig. 3E).

5.2. Metasomatic and hydrothermal facies

Two types of fenite alteration, which are referred to as silicocarbonatites (Demaiffe, 2008), have been recognized at the contact between the carbonatites and the Karagwe-Ankolan metasediments: biotite-bearing fenite and K-feldspar-bearing fenite (Fig. 3F). The latter occurs as replacement of the mica-bearing facies. In the biotite-bearing fenite, biotite shows well-developed crystals up to 2 cm in size (see Supplementary data, Fig. 3G). Biotite is partly transformed into phlogopite (see Supplementary data), both phyllosilicates being in turn replaced by feldspars (mainly K-feldspar, with accessory albite grains). Other associated minerals are titanite, richterite, calcite and apatite. In K-feldspar-bearing fenite, feldspar constitutes up to 70% of the rock volume, and occurs associated with biotite, zircon, rutile and pyrochlore.

Table 1
Major element contents (in wt.%) of samples from the Matongo carbonatites.

Sample	Description	SiO_2	Al_2O_3	$Fe_2O_{3(tot)}$	MnO	MgO	CaO	Na_2O	K_2O	TiO_2	P_2O_5	LOI	Sum
LT-SI-1	Sövite I	0.09	0.01	0.03	0.686	0.4	54.13	0.03	0.01	0.001	0.01	#N.A.	79.77
RG140.276-S7/62-63m	Sövite I	0.08	0.01	0.03	0.682	0.5	55.16	0.02	0.01	0.001	0.01	#N.A.	80.97
Gi3-ITS4/84-87m	Sövite II	0.88	4.88	1.14	0.25	0.49	51.72	0.08	0.03	0.01	1.42	38.16	99.06
LT-SII-1	Sövite II	2.42	0.7	1.33	0.134	0.47	50.99	0.41	0.04	0.014	0.62	34.64	80.76
RG 140.273	Sövite II	0.93	0.26	2.21	0.221	0.11	56.92	0.08	0.15	0.008	0.41	34.12	84.71
Gi2-S3/147	Sövite II	10.27	0.96	4.48	0.131	2.26	42.9	1.47	0.48	0.377	3.77	22.5	81.33
Gi12-S5/121.5m	Sövite II with apatite	1.32	0.01	1.36	0.23	0.75	48.57	0.2	0.07	0.04	10.45	36.19	99.19
LT-cum-1	Sövite II with apatite and px	23	1.77	11.37	0.183	3.44	31.39	2.85	1.17	0.377	2.46	24.99	97.54
RG 140.280A-S5/121-121.60m	Sövite II with apatite and px	28.74	1.35	16.65	0.088	2.44	25.57	5.37	0.29	0.339	10.39	9.08	98.11
Gi1-S2/171-172m	Sövite II with apatite and px	6.46	0.68	3.27	0.17	0.62	42.82	0.28	0.44	0.10	3.36	40.39	98.59
Gi10-S6/155-156m	Sövite II with apatite and px	6.28	0.54	4.27	0.16	0.61	42.74	0.59	0.34	0.11	4.79	38.30	98.73
Gi11-S8/56m	px and apatite cumulate	21.48	3.22	10.40	0.09	1.74	34.48	0.81	2.36	0.40	9.96	15.61	100.55
RG 140.280B-S5/121-121.60m	Sövite II with apatite and amph.	16.18	0.61	7.76	0.061	1.29	38.03	3.4	0.43	0.165	19.29	5.02	89.44
Gi16-S3/121m	Ferrocarbonatite	7.72	2.28	9.46	0.21	3.17	29.68	0.65	0.09	0.47	0.28	32.58	54.01
LT-CJ-1	Ferrocarbonatite	2.31	1.21	2.19	0.268	0.68	50.49	0.05	0.34	0.037	3.91	28.38	83.73
RG 140.272-ITS5/60m	Ferrocarbonatite	9.39	2.82	4.11	1.045	2.49	44.62	0.03	0.89	0.389	0.24	38.33	85.68
Gi17-S7/91-95	"late" hydrothermal calcite	0.91	0.26	1.22	0.619	2.47	50.24	0.03	0.12	0.032	0.03	11.03	82.97
Gi5-ITS3/291	kfs–fenite	51.78	14.5	0.67	0.064	0.09	10.67	0.71	12.24	0.027	0.11	16.49	99.54
Gi14-ITS4/150	kfs–fenite	32.06	9.35	2.14	0.478	0.37	25.39	0.95	7.15	0.02	0.15	13.21	88.89
Gi15-S5/104-106	bt–fenite	35.26	16.55	7.9	0.098	4.64	13.19	4.47	3.54	1.972	0.14	6.56	98.3
S1/183.5-184.25	kfs–bt–fenite	55.04	16.79	2.32	0.105	0.41	6.06	0.91	12.56	0.176	0.63	#N.A.	100.4

Feldspar crystals are present as grains with amoeboidal boundaries or form cm-long lath-shaped aggregates.

"Late" hydrothermal calcite has been identified in association which sövite I. It occurs as veinlets containing very fine-grained calcite (several tens of μm in size), slightly enriched in Fe, Mn and Mg (up to 1.2 wt.%FeO, 0.7 wt.% MgO and 0. 6 wt.% MnO) and coated by iron oxides.

6. Geochemistry

6.1. Major and trace element composition (Tables 1–3)

As expected from the mineralogy, the Matongo carbonatites plot in the sövite and ferrocarbonatite fields of the ternary CaO-MgO-Fe_2O_3(t)+MnO diagram of Le Maitre (2002) (Fig. 4A). The sövite I samples, which consist essentially of pure calcite, plot close to the CaO apex of the triangle. Their MnO, MgO and $Fe_2O_{3(t)}$ concentration is very low: ~0.7 wt.%, ~0.5 wt.% and <1 wt.% respectively. Their SiO_2 and Al_2O_3 concentration is also very low, <0.1 wt.%. The sövite II samples are characterized by a wide range of CaO concentrations (25.6–56.9 wt.%) that are inversely correlated with the SiO_2 (0.9–28.7 wt.%), Fe_2O_3 (1.1–16.6 wt.%) and Na_2O (0.1–5.4 wt.%) concentrations. The samples define a rough trend extending from the typical sövite to the ferrocarbonatite field. In the $Na_2O + K_2O$–MgO + Fe_2O_3(t)–CaO ternary diagram (Fig. 4B; Le Bas, 1984), the Matongo sövites define an elongated trend that can be related to clinopyroxene and/or amphibole fractional crystallization during carbonatite magma uprise and emplacement. Ferrocarbonatites also display a wide range of CaO concentrations (29.7–50.5 wt.%) that are inversely correlated with the Fe_2O_3 and MgO contents (1.2–9.5 wt.% and 0.7–3.2 wt.%, respectively). Fe and Mg enrichments are likely linked to ankerite and dolomite formation. The "late" hydrothermal calcite is characterized by geochemical features close to sövites (50.2 wt.% CaO, 2.5 wt.% MgO, 1.2 wt.% Fe_2O_3 and0.6 wt.% MnO). The fenites occur quite scattered in the $Na_2O + K_2O$–MgO + Fe_2O_3(t)–CaO ternary diagram (Fig. 4B; Le Bas, 1981, 1984). They show a trend that likely represents a consequence of alkali enrichment of the host country rocks (feldspathoidal syenite and metasediments) during the fenitization processes.

The chondrite-normalized rare-earth element (REE) abundance patterns of the various carbonatite facies are heterogeneous (Fig. 5). The sövite I samples have a rather low total REE abundance (ΣREE: 4–8 ppm) and display flat REE patterns with rather low La_N/Yb_N ratios (3.1–4). The sövite II samples and the clinopyroxene-apatite cumulates (less commonly amphibole cumulates) are strongly enriched in REE (ΣREE from 442 up to 1550 ppm), with a significant LREE enrichment (La_N/Yb_N ranging from 49 to 175) but no significant Eu anomaly ($Eu/Eu^* > 0.8$). The ferrocarbonatites are similar to the sövites II ($225 < \Sigma REE < 1048$ ppm, $17 < La_N/Yb_N < 64$ and $0.8 < Eu/Eu^* < 0.9$). The fenites are also largely similar with ΣREE concentrations varying between 134 and 681 ppm, with LREE-enrichment ($25 < La_N/Yb_N < 46$) and no significant Eu anomaly. The "late" hydrothermal calcite is also enriched in REE (ΣREE = 397 ppm), but displays a peculiar pattern characterized by LREE depletion ($La_N/Sm_N = 0.4$) and well-marked MREE-hump, with a small Eu negative anomaly ($Eu/Eu^* = 0.8$) and a tetrad effect ($(La_N * Sm_N)/(Ce_N * Nd_N) = 2.3$).

Primitive mantle-normalized spidergram patterns (Fig. 6) illustrate that most of the Matongo carbonatite and fenite rocks share common characteristics: (1) an overall enrichment compared to the primitive mantle, except for the sövites I; (2) a general enrichment in large-ion lithophile elements (LILE) relatively to high-field-strengh elements (HFSE), in particular for the fenites; (3) negative anomalies in Ti, Zr, Hf (and K for the sövites and ferrocarbonatites); and (4) variable enrichments in Th, U, Nb and Ta that can be related to the presence of Nb(-Ta)-rich oxides (pyrochlore, magnetite) and U–Th-bearing minerals (pyrochlore). In general, the patterns observed are quite comparable to the "world average carbonatite" (Chakhmouradian, 2006), except for Th, U, Nb and Ta. It should be mentioned that sövite I samples display atypical patterns, with low global enrichment close to the primitive-mantle level, together with positive Sr and Th anomalies and a negative Ti anomaly.

Table 2
REE contents (ppm) La_N/Yb_N ratios, ΣREE and tetrad effect of samples from the Matongo carbonatites.

Sample	Description	La	Ce	Pr	Nd	Sm	Eu	Gd	Tb	Dy	Ho	Er	Yb	Lu	La_N/Yb_N	Eu^*/Eu	SumREE	Tetrad effect (LaN * SmN)/(CeN * NdN)
LT-SI-1	Sövite I	0.6	1.1	0.18	0.8	0.3	0.06	0.2	0.1	0.2	0.1	0.1	0.1	0.04	4.05	0.71	3.88	1.6
RG140.276	Sövite I	1.4	1.9	0.37	1.7	0.8	0.17	0.7	0.1	0.5	0.1	0.3	0.3	0.05	3.15	0.68	8.39	2.8
Gi3-ITS4/84-87m	Sövite II	146	275		101	12	3.21		0.91				1.47	0.24	67.1	1.47	539	0.5
LT-SII-1	Sövite II	156	250	25	86	12	3.19	9.7	0.9	4.3	0.8	2.2	1.9	0.28	55.5	0.89	552	0.7
RG 140.273	Sövite II	129	213	21.4	71	10	2.4	7.2	0.7	3.2	0.6	1.6	1.5	0.23	58.1	0.84	461	0.7
Gi2-S3/147	Sövite II	237	411	45	157	22	5.77	15.9	1.5	6.3	1	2.7	1.8	0.26	89.0	0.91	907	0.6
Gi12-S5/121.5m	Sövite II with apatite	188	365		131	16	4.25		1.23				2.16	0.32	58.8	1.46	707	0.5
LT-cum-1	Sövite II with apatite and px	114	203	21.1	76	11	2.66	6.5	0.8	3.7	0.6	1.6	1.3	0.22	59.3	0.92	442	0.6
RG 140.280A	Sövite II with apatite and px	239	432	48.2	171	24	6	16	1.5	6.3	1	2.8	2.1	0.33	76.9	0.89	950	0.6
Gi1-S2/171-172m	Sövite II with apatite and px	210	407		160	20	5.71		1.51				1.77	0.28	80.2	1.49	807	0.5
Gi10-S6/155-156m	Sövite II with apatite and px	132	261		97	12	3.42		1.05				1.82	0.26	49.0	1.49	509	0.5
Gi11-S8/56m	px and apatite cumulate	170	329		119	14	3.83		1				1.22	0.19	94.2	1.47	638	0.5
RG 140.280B	Sövite II with apatite and amph.	415	719	76.2	262	33	8.09	22.7	1.8	7	1.1	2.6	1.6	0.24	175.3	0.86	1550	0.6
Gi16-S3/121m	Ferrocarbonatite	145	291		112	14	3.89		1.03				1.52		64.5	1.48	568	0.5
LT-CJ-1	Ferrocarbonatite	292	476	48.8	163	23.9	6.06	17.8	1.9	8.6	1.5	4.1	3.1	0.49	63.7	0.86	1047	0.7
RG 140.272	Ferrocarbonatite	62.5	92.9	9.78	35	6.7	1.67	5.4	0.7	3.9	0.8	2.3	2.5	0.41	16.9	0.82	225	1.0
Gi17-S7/91-95	"Late" hydrothermal calcite	31.4	72.9	12.8	76.2	50.7	17.2	75.5	10.1	32.5	3.7	6.4	5.8	0.87	3.66	0.85	396	2.3
Gi5-ITS3/291	kfs-fenite	38.3	62.2	6.19	19.1	2.4	0.67	2.1	0.2	1	0.2	0.7	0.7	0.11	37.0	0.89	134	0.6
Gi14-ITS4/150	kfs-fenite	188	310	30.2	97.5	15.3	4.53	12.8	1.6	8.2	1.8	5	5	0.74	25.4	0.96	681	0.8
Gi15-S5/104-106	bt-fenite	54.3	113	14.1	55.2	8.6	2.35	5.7	0.7	2.7	0.4	1.1	0.8	0.15	45.9	0.97	259	0.6
S1/183.5-184.25	kfs-bt-fenite	54.6	107	11.7	42.5	6.4	1.65	4.2	0.6	2.9	0.5	1.3	1	0.12	36.9	0.92	234	0.6
Normalization values used in REE diagrams – chondrite concentrations of Sun (1982) and McDonough (1990)		0.31	0.81	0.12	0.60	0.20	0.07	0.26	0.05	0.32	0.07	0.21	0.21	0.03				

6.2. U–Th–Pb data of the Matongo and Lueshe zircon megacrysts

Zircon megacrysts selected for U–Th–Pb geochronology were 1–6 mm in size, euhedral to subeuhedral (with the prevailing presence of the (101) pyramids; Fransolet and Tack, 1992) and frequently show oscillatory zoning (Fig. 7A–D). The zoning can be related to variations in Th (up to 0.34 and 2.2 wt.% ThO_2 for Matongo and Lueshe zircon, respectively), U (up to 0.12 and 0.09 wt.% UO_2, respectively) and Hf (0.36–0.90 and 0.39–1.45 wt.%, respectively) contents. The inner zones of the zircons often show darker luminescence colours, whereas in many grains the primary zoning is replaced by cloudy to irregular patchy CL patterns related to alteration. The primary zoning has commonly been obliterated, from inside to outside, probably by a fluid phase entering the grains via small cracks. Sometimes the entire grain is affected. The altered CL dark (low-luminescence) areas are characterized by lower total oxides (ca. 95 wt.%), higher U and Th contents, and detectable concentrations of Ti, Al, P, Ca, Mn and Fe (up to 1 wt.% each), whereas the alteration domains with bright luminescence patterns differ by having low Th and U concentrations, often below detection limit of the EPMA (see Table 4).

Results of U–Th–Pb isotope analyses on zircon megacrysts from Matongo (sample RGM 9672) and Lueshe (sample RGM 9673) are presented in Fig. 7E and F and Table 5. Laser spots were set predominantly on the primary, oscillatory-zoned domains. Altered areas were also analyzed: spots A36-A38 for Matongo and A19-A27 for Lueshe zircon. Within analytical error, the results were, however, in both cases – indistinguishable from those of the primary oscillatory domains, except for the slightly discordant analysis A37.

Seventeen U–Pb measurements on three zircon megacrysts from Matongo are equivalent and concordant. They yield a concordia age of 705.5 ± 4.5 Ma (Fig. 7E), significantly younger than the Pb-evaporation age of 738 ± 4 Ma (Tack et al., 1995). The 705 Ma age is consistent with the weighted average $^{206}Pb/^{238}U$ and $^{208}Pb/^{232}Th$ ages of 705.2 ± 4.6 Ma and of 697.3 ± 5.3 Ma, respectively.

In the case of Lueshe, twenty-two U–Pb analyses on three megacrysts also give equivalent and concordant values with a Concordia age of 798.5 ± 4.9 Ma (Fig. 7F). This is consistent with the corresponding weighted average $^{206}Pb/^{238}U$ and $^{208}Pb/^{232}Th$ ages of 801.0 ± 3.9 Ma and of 802.5 ± 4.0 Ma, respectively.

7. Discussion

7.1. Magmatic processes and sources

Petrographic observations and geochemical data illustrate that different magmatic processes took place during the emplacement of the Matongo carbonatite: (i) fractionation of clinopyroxene + apatite during carbonatite emplacement; (ii) ankerite formation during late-stage carbonatite intrusion; and (iii) alkali loss inducing metasomatic fenitisation and the formation of silicocarbonatites. These processes are recorded in the sövites II, the ferrocarbonatite and the fenite (silicocarbonatite), which share similar geochemical characteristics. These rocks show LREE and LILE enrichments and similar Sr and Nd isotopic compositions. The initial $^{87}Sr/^{86}Sr$ varies between 0.7028 and 0.7040 and initial εNd values between +0.2 and +5.2 (Demaiffe, 2008; Table 6). These values plot in the mantle array (Fig. 8) and point to a mantle source that is less depleted than the DM (Demaiffe, 2008). The Matongo isotopic compositions are comparable to those reported for Lueshe sövites, recalculated to 800 Ma (Kramm et al., 1997). This suggests that a similar source has been sampled for the two carbonatite magmas, despite a difference in emplacement age of ca. 100 Ma. A long-lived

Table 3
Trace elements (in ppm) of samples from the Matongo carbonatite.

Sample	Rb	Ba	Th	U	Nb	Ta	K	La	Ce	Pb	Pr	Sr	Nd	Zr	Hf	Sm	Eu	Ti	Gd	Tb	Dy	Y	Ho	Er	Yb	Lu
LT-SI-1	2	8	0.6	0.1	1	0.1	0.01	0.6	1.1	5	0.18	2499	0.8	21	0.4	0.3	0.06	0.00	0.2	0.1	0.2	4	0.1	0.1	0.1	0.04
RG140.276	2	10	1.8	0.1	1	0.1	0.01	1.4	1.9	5	0.37	1531	1.7	11	0.2	0.8	0.17	0.00	0.7	0.1	0.5	5	0.1	0.3	0.3	0.05
Gi3-ITS4/84-87m	11.00	816	10.1	0.5	11.0	6.20	0.02	146	275			5256	101			11.6	3.21	0.00		0.91					1.47	0.24
LT-SII-1	<2	734	1.9	0.5	8.0	0.4	0.02	156	250	5	25	6801	86	88	0.9	11.7	3.19	0.01	9.7	0.9	4.3	25	0.8	2.2	1.9	0.28
RG 140.273	3	920	0.4	0.2	10.0	0.1	0.09	129	213	5	21.4	9385	71	16	0.2	9.8	2.4	0.00	7.2	0.7	3.2	21	0.6	1.6	1.5	0.23
Gi2-S3/147	22	563	11.7	0.7	88.0	4.9	0.29	237	411	6	45	4492	157	49	0.4	21.8	5.77	0.16	15.9	1.5	6.3	30	1	2.7	1.8	0.26
Gi12-S5/121.5m	<4	558			10.0		0.04	188	365			6512	131			15.5	4.25	0.02		1.23					2.16	0.32
LT-cum-1	70	394	3.6	2.7	55.0	5	0.70	114	203	5	21.1	3560	76	226	1.4	10.5	2.66	0.16	6.5	0.8	3.7	17	0.6	1.6	1.3	0.22
RG 140.280A	4	162	16.8	14.4	168.0	13.4	0.17	239	432	23	48.2	2380	171	332	2.3	23.7	6	0.15	16	1.5	6.3	28	1	2.8	2.1	0.33
Gi1-S2/171-172m	22	553	2.8	16.3	31.0	5.3	0.26	210	407			4237	160			20.3	5.71	0.04		1.51					1.77	0.28
Gi10-S6/155-156m	14.0	591	15.6	5.4	47.0	4.03	0.20	132	261			4105	97			12.2	3.42	0.05		1.05					1.82	0.26
Gi11-S8/56m			2.83	44.0	2424	20.4	1.41	170	329			1916	119			13.8	3.83	0.17		1					1.22	0.19
RG 140.280B	7	301	24.2	3.8	86	6.2	0.26	415	719	7	76.2	4955	262	339	4.4	32.8	8.09	0.07	22.7	1.8	7	31	1.1	2.6	1.6	0.24
Gi16-S3/121m			7.8	4.8	57	5.3	0.05	145	291			3601	112			14	3.89	0.21		1.03					1.52	
LT-CJ-1	20	203	22.6	0.7	45	0.1	0.20	292	476	18	48.8	1843	163	32	0.6	23.9	6.06	0.02	17.8	1.9	8.6	45	1.5	4.1	3.1	0.49
RG 140.272	116	443	50.5	1.4	74	1.9	0.53	62.5	92.9	20	9.78	558	35	54	0.8	6.7	1.67	0.17	5.4	0.7	3.9	27	0.8	2.3	2.5	0.41
Gi17-S7/91-95	10	793	2000	4.6	10	0.1	0.07	31.4	72.9	38	12.8	1280	76.2	33	0.8	50.7	17.2	0.01	75.5	10.1	32.5	90	3.7	6.4	5.8	0.87
Gi5-ITS3/291	289	1437	11.8	158	461	56.3	7.34	38.3	62.2	61	6.19	1955	19.1	200	1.6	2.4	0.67	0.01	2.1	0.2	1	7	0.2	0.7	0.7	0.11
Gi14-ITS4/150	150	1469	13.7	43.1	1000	17.7	4.29	188	310	33	30.2	4572	97.5	21	0.4	15.3	4.53	0.01	12.8	1.6	8.2	47	1.8	5	5	0.74
Gi15-S5/104-106	125	1353	16.8	0.7	54	7.7	2.12	54.3	113	5	14.1	1243	55.2	216	4.7	8.6	2.35	0.86	5.7	0.7	2.7	9	0.4	1.1	0.8	0.15
S1/183.5-184.25	206	2236	7.7	7.7	580	19.2	7.53	54.6	107	8	11.7	669	42.5	16	0.2	6.4	1.65	0.08	4.2	0.6	2.9	14	0.5	1.3	1	0.12
Normalization values used in spidergrams – primitive mantle concentrations of McDonough et al. (1992)	*0.635*	*6.989*	*0.085*	*0.021*	*0.713*	*0.041*	*0.0301*	*0.687*	*1.775*	*0.185*	*0.276*	*21.1*	*1.25*	*11.2*	*0.309*	*0.444*	*0.154*	*0.217*	*0.544*	*0.099*	*0.674*	*4.55*	*0.149*	*0.438*	*0.493*	*0.068*

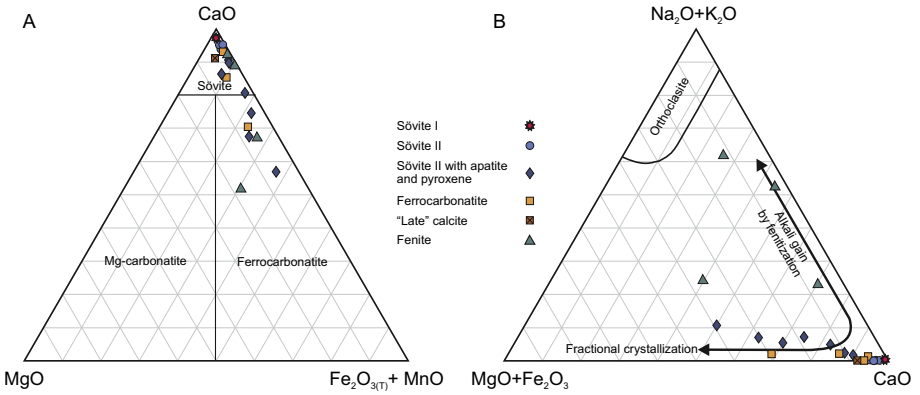

Fig. 4. The Matongo carbonatites in classification/discrimination ternary diagrams: (A) CaO–Fe_2O_3(t) + MnO–MgO (based on Le Maitre, 2002) and (B) $Na_2O + K_2O$–CaO–MgO + Fe_2O_3 (Le Bas, 1981, 1984).

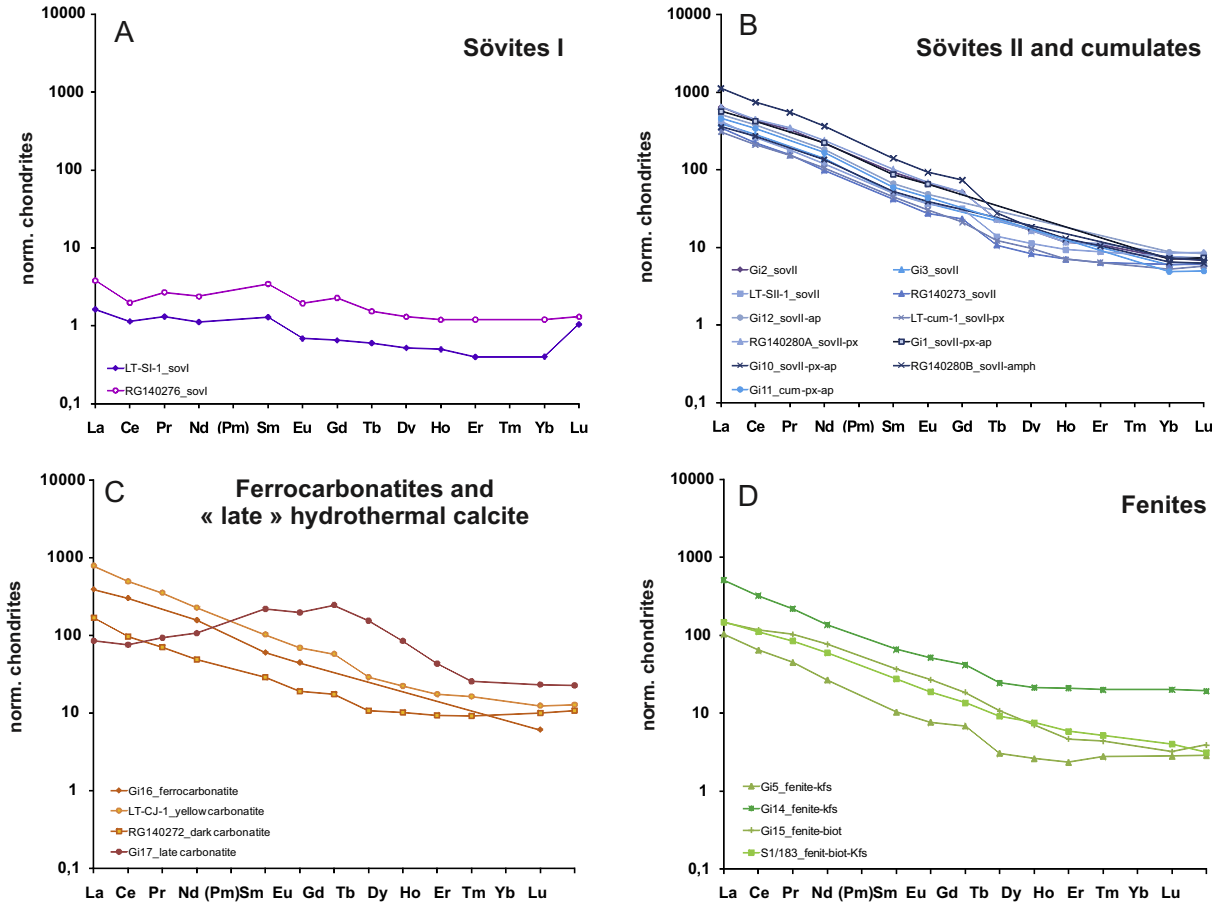

Fig. 5. Chondrite-normalized REE abundance patterns of the Matongo carbonatite facies. (A) sövite I, (B) sövite II and associated cumulates (comprising clinopyroxene, apatite and amphibole), (C) ferrocarbonatite and "late" hydrothermal calcite, and (D) fenites-silicocarbonatites. Normalization values to the chondrites from Sun (1982) and McDonough (1990).

thermal anomaly could thus have persisted in the mantle beneath Central Africa. The Neoproterozoic Matongo and Lueshe carbonatites differ from the young (< 200 Ma) East African carbonatites (Bell and Tilton, 2001), whose isotopic field is displaced towards lower εNd values and which show extended range of Sr isotopic compositions. Their field extends between the HIMU and EMI fields and reflects the heterogeneity of the young East African carbonatite source. Several interpretations have been proposed to explain this heterogeneity: (i) The lithospheric mantle itself is heterogeneous and results from enrichment and/or depletion processes at different times and degrees (Kalt et al., 1997); (ii) Various fluid or melt incursions influenced the lithosphere, at least since the Proterozoic (Bell and Tilton, 2001); (iii) Upwelling of a mantle cell or plume of HIMU affinities resulted in a recently metasomatized EMI-type lithosphere (Bell and Simonetti, 1996); (iv) The EMI-HIMU mixing trend could be due to the signature of a heterogeneous mantle plume

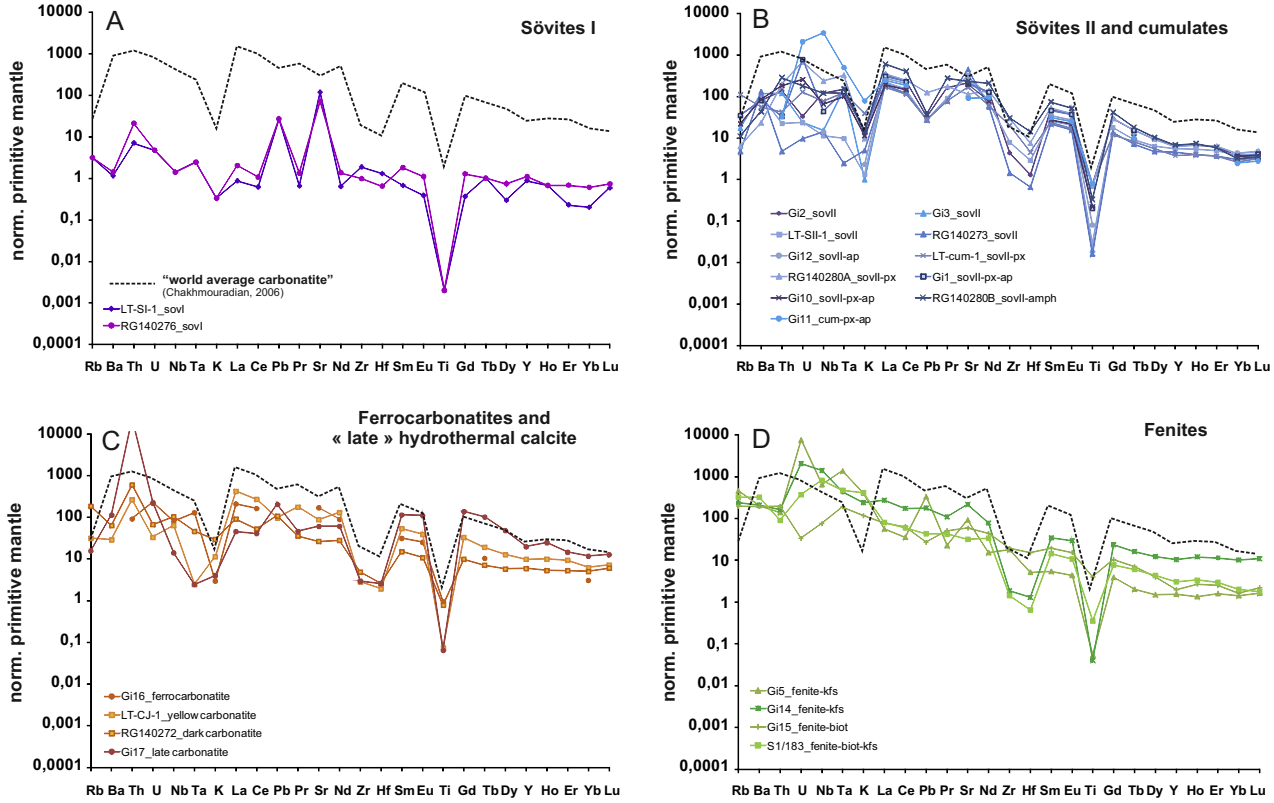

Fig. 6. Spidergrams of the Matongo carbonatite facies. (A) sövite I, (B) sövite II and associated cumulates (comprising clinopyroxene, apatite and amphibole), (C) ferrocarbonatite and "late" hydrothermal calcite, and (D) fenites-silicocarbonatites. Normalization values to the primitive mantle from McDonough et al. (1992).

carrying these components from the deep mantle (Bell and Tilton, 2001).

In terms of isotopic compositions, the Proterozoic carbonatites of Matongo, Lueshe and Deerdepoort (1340 Ma, South Africa; Verwoerd, 1967) constitute a rather homogeneous group, significantly different from the recent East African carbonatites, in particular for their higher εNd values. The mantle source sampled during the Proterozoic by carbonatitic magmas is likely a deep-seated homogeneous reservoir, possibly contaminated by lithospheric material rather than a heterogeneous lithosphere as proposed for the African carbonatites by Bell and Tilton (2001). However, to confirm this statement complementary analyses of different Proterozoic African carbonatites are needed.

7.2. Late hydrothermal processes

The geochemical and isotopic characteristics of the sövite II and the ferrocarbonatites, which represent the largest part of the Matongo carbonatite, are clearly distinct from the sövite I and the "late" hydrothermal calcite. The sövite I was sampled in a deformed zone with macroscopic fractures. The "late" calcite occurs as thin veins of hydrothermal origin crosscutting the sövite I (Midende, 1984). Both rock types show petro-geochemical evidence of interaction with hydrothermal fluids. They display peculiar REE patterns with LREE fractionation. In addition, the late calcite (sample Gi17) shows intra-REE fractionation with a significant tetrad effect resulting from the interaction with fluids (Bau, 1996). Also, the very low REE content of sövite samples, illustrated by flat patterns (1 to 5 times the chondrites; Fig. 5), is hardly explicable by magmatic processes. Similarly, the Sr and Nd isotope compositions of the "late" calcite ($^{87}Sr/^{86}Sr(i) = 0.71425$ and $\varepsilon Nd(i) = -44$; Fig. 8) suggest the hydrothermal introduction of radiogenic Sr and non-radiogenic Nd from the surrounding country rocks. Moreover, the non-radiogenic signature of the Nd isotope composition indicates disturbance of the Sm–Nd system, possibly during interaction with fluids. The particularly low enrichment, if any, of the sövite I in REE and other trace elements indicates that this rock has been altered after the carbonatite emplacement.

Despite the close spatial association of the sövite I and late hydrothermal calcite, the precise relationships between the REE signatures of these facies still remain incomplete. The timing of hydrothermal fluid circulation responsible for the observed alteration is also not well constrained. However, hot fluids could have circulated during a quite long time span after magmatic intrusion, as illustrated by long-lived (10–30 Ma) hydrothermal systems associated with large granites (e.g. Kontak and Clark, 2002; Zhao et al., 2004).

7.3. Geodynamic setting of the carbonatite emplacement

7.3.1. Significance of the zircon megacryst ages

Zircon megacrysts are well-known in carbonatitic systems (e.g. Caruba and Iacconi, 1983; Hoskin and Schaltegger, 2003). In the URAPC, the occurrence of the zircon megacrysts close to the Matongo carbonatite and their ubiquitous primary calcite, magnesian calcite, and nahcolite inclusions (Burke, 1998) obviously argue for the carbonatitic affinity of these minerals, as already proposed by Fransolet and Tack (1992). The latter authors related the crystallization of these zircons to the circulation of alkaline pegmatitic fluids in the URAPC system. Regardless of the exact origin of these zircon grains (magmatic vs. hydrothermal), their crystallization is associated with the carbonatite and, thus, the U–Pb age that

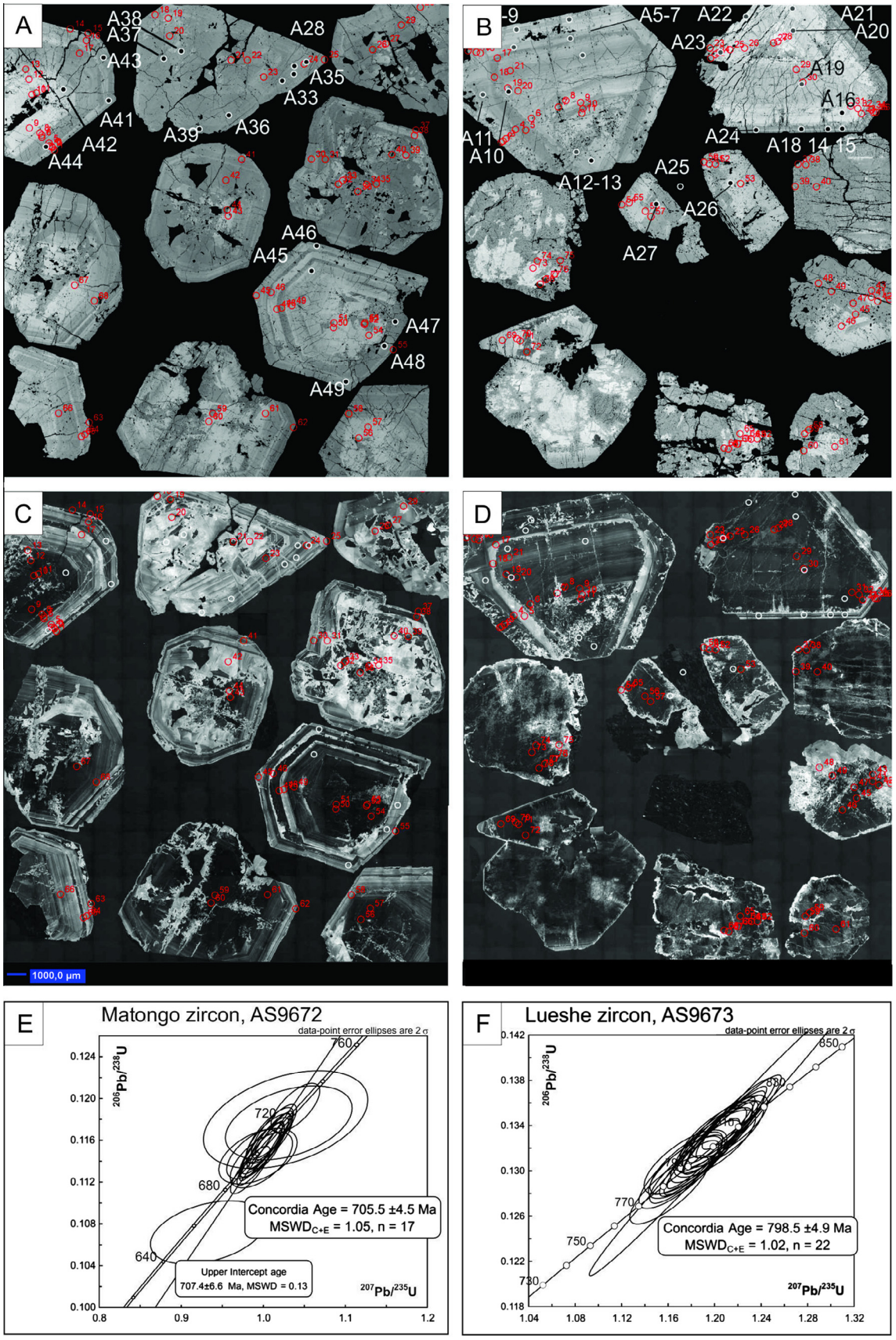

Fig. 7. Pictures of the Matongo (A and C) and Lueshe (B and D) zircon megacrysts (A and B: backscattered electron images, C and D: cathodoluminescence images): red and white dots represent electron microprobe and LA–MC–ICP–MS analyses, respectively. E and F: concordia plots of LA–MC–ICP–MS U–Pb data, with data point error ellipses at 2σ. (For interpretation of the references to colour in this figure legend, the reader is referred to the web version of this article.)

Table 4
Representative electron probe microanalyses of zircon megacrysts from Lueshe and Matongo.

	Matongo (RGM 9672)									Lueshe (RGM 9673)									
Grain	1	1	2	3	4	6	6	9	10	1	1	2	3	4	4	6	7	9	10
Analysis	2	17	20	27	35	47	51	63	67	4	8	25	40	45	48	56	61	69	76
CL brightness	None	Bright	Bright	None	Bright	None	None*	None	None	Bright	None	None	None*	None*	Bright	None	None	None	Medium
wt.%																			
SiO_2	33.18	32.78	33.05	33.01	32.89	32.88	30.39	33.11	32.96	33.05	32.91	32.79	28.12	30.41	32.91	32.66	32.66	32.40	32.71
ZrO_2	66.45	65.68	67.19	66.23	66.31	66.35	61.96	65.82	65.53	66.19	65.92	64.65	57.10	61.58	65.87	65.19	65.37	65.77	65.71
HfO_2	0.53	0.67	0.60	0.71	0.67	0.62	0.66	0.36	0.70	0.40	0.62	0.58	0.70	0.41	1.25	0.43	0.69	0.59	0.63
ThO_2	0.137	<d.l.	<d.l.	0.087	<d.l.	0.098	0.309	0.136	0.270	<d.l.	0.171	1.151	1.198	0.699	<d.l.	0.463	0.429	0.257	0.535
UO_2	0.059	<d.l.	<d.l.	0.043	<d.l.	0.041	0.108	0.044	0.066	<d.l.	<d.l.	<d.l.	<d.l.	<d.l.	<d.l.	<d.l.	<d.l.	0	0
PbO	<d.l.	<d.l.	<d.l.	<d.l.	<d.l.	<d.l.	<d.l.	<d.l.	<d.l.	<d.l.	<d.l.	<d.l.	<d.l.	<d.l.	<d.l.	<d.l.	<d.l.	0	0
P_2O_5	<d.l.	<d.l.	<d.l.	<d.l.	<d.l.	<d.l.	<d.l.	<d.l.	<d.l.	<d.l.	<d.l.	<d.l.	0.120	<d.l.	<d.l.	<d.l.	<d.l.	0	0
TiO_2	<d.l.	<d.l.	<d.l.	<d.l.	<d.l.	<d.l.	0.145	<d.l.	<d.l.	<d.l.	<d.l.	<d.l.	0.652	0.222	<d.l.	<d.l.	<d.l.	0	0
Al_2O_3	<d.l.	<d.l.	<d.l.	<d.l.	<d.l.	<d.l.	0.356	<d.l.	<d.l.	<d.l.	<d.l.	<d.l.	0.854	0.411	<d.l.	<d.l.	<d.l.	0	0
CaO	0.031	<d.l.	<d.l.	<d.l.	<d.l.	<d.l.	0.539	<d.l.	0.057	<d.l.	<d.l.	<d.l.	1.362	0.740	<d.l.	<d.l.	<d.l.	0	0
MnO	<d.l.	<d.l.	<d.l.	<d.l.	<d.l.	<d.l.	0.133	<d.l.	<d.l.	<d.l.	<d.l.	<d.l.	0.237	0.084	<d.l.	<d.l.	<d.l.	0	0
FeO	<d.l.	<d.l.	<d.l.	<d.l.	<d.l.	<d.l.	0.715	<d.l.	0.059	<d.l.	<d.l.	0.0314	0.668	0.761	<d.l.	<d.l.	<d.l.	0	0
Total	100.39	99.13	100.85	100.08	99.88	99.99	95.31	99.48	99.64	99.64	99.62	99.20	91.01	95.32	100.04	98.74	99.15	99.02	99.58
Cations per formula units																			
Si	1.009	1.009	1.002	1.007	1.006	1.005	0.981	1.013	1.010	1.010	1.008	1.013	0.954	0.981	1.007	1.010	1.007	1.002	1.006
Zr	0.985	0.985	0.993	0.986	0.989	0.989	0.975	0.982	0.980	0.986	0.985	0.974	0.945	0.969	0.983	0.983	0.983	0.991	0.985
Hf	0.005	0.006	0.005	0.006	0.006	0.005	0.006	0.003	0.006	0.003	0.005	0.005	0.007	0.004	0.011	0.004	0.006	0.005	0.006
Th	0.001			0.001		0.001	0.002	0.001	0.002		0.001	0.008	0.009	0.005		0.003	0.003	0.002	0.004
U	0.000			0.000		0.000	0.001	0.000	0.000									0	0
Pb																		0	0
P													0.003					0	0
Ti							0.004						0.017	0.005				0	0
Al							0.014						0.034	0.016				0	0
Ca	0.001						0.019		0.002				0.050	0.026				0	0
Mn							0.004						0.007	0.002				0	0
Fe							0.019		0.002			0.001	0.019	0.021				0	0
Total	2.001	2.000	2.000	2.000	2.000	2.000	2.024	2.000	2.002	2.000	2.000	2.000	2.045	2.028	2.000	2.000	2.000	2.000	2.000

* Metamict area.

Table 5
Representative U–Th–Pb analyses of zircon megacrysts from Lueshe and Matongo.

		^{207}Pb[a] (cps)	U[b] (ppm)	Pb[b] (ppm)	Th[b] U	^{206}Pbc[c] (%)	^{206}Pb[d] ^{238}U	±2s (%)	^{207}Pb[d] ^{235}U	±2s (%)	^{208}Pb ^{232}Th	±2s (%)	^{207}Pb[d] ^{206}Pb	±2s (%)	rho[e]	^{206}Pb ^{238}U	±2s (Ma)	^{207}Pb ^{235}U	±2s (Ma)	^{208}Pb ^{232}Th	±2s (Ma)	^{207}Pb ^{206}Pb	±2s (Ma)	conc.[f] (%)
Lueshe (RGM 9673)	Spot AS9673																							
	A05	27607	127	88	18	0.06	0.13070	1.7	1.176	2.2	0.0407	1.7	0.06524	1.3	0.78	792	13	789	12	806	13	782	28	101
	A06	35006	158	130	22	0.07	0.12990	1.7	1.174	2.1	0.0406	1.6	0.06553	1.1	0.84	787	13	788	11	805	13	792	23	99
	A07	15462	68	200	87	0.14	0.13320	1.8	1.206	2.4	0.0413	1.6	0.06565	1.6	0.75	806	14	803	14	818	13	795	34	101
	A08	12161	56	92	47	0.09	0.13080	1.8	1.175	2.5	0.0408	1.6	0.06516	1.7	0.72	792	13	789	14	808	13	780	36	102
	A09	16321	74	220	90	0.18	0.13240	1.8	1.200	2.4	0.0408	1.7	0.06574	1.5	0.77	802	14	801	13	808	14	798	32	100
	A10	23555	112	94	24	0.16	0.12830	1.9	1.161	2.4	0.0403	1.9	0.06562	1.4	0.80	778	14	782	13	799	15	794	30	98
	A11	13565	64	140	65	0.14	0.12990	2.0	1.171	2.5	0.0409	1.7	0.06538	1.5	0.80	787	15	787	14	809	14	786	31	100
	A12	131214	590	160	5	0.10	0.13410	1.8	1.214	2.0	0.0401	1.7	0.06564	0.9	0.90	811	14	807	11	795	14	795	18	102
	A13	168214	752	210	5	0.05	0.13360	1.8	1.206	2.0	0.0399	1.7	0.06546	0.8	0.91	808	14	803	11	791	13	789	17	102
	A14	36520	164	150	26	0.11	0.13270	1.8	1.200	2.2	0.0398	1.7	0.06559	1.3	0.81	803	13	801	12	788	13	793	27	101
	A15	25933	119	100	24	0.18	0.13040	1.8	1.176	2.3	0.0398	1.8	0.06543	1.5	0.77	790	13	789	13	789	14	788	31	100
	A16	80661	326	580	49	0.05	0.13300	2.8	1.202	2.9	0.0403	2.1	0.06557	0.9	0.95	805	21	802	16	799	16	793	19	102
	A17	32685	154	220	42	0.10	0.13170	1.7	1.192	2.1	0.0398	1.6	0.06565	1.2	0.82	798	13	797	12	789	13	795	25	100
	A18	51116	234	200	24	0.09	0.13310	1.8	1.203	2.1	0.0403	1.6	0.06551	1.1	0.85	806	13	802	12	798	13	791	23	102
	A19	38178	179	230	37	0.11	0.13280	1.7	1.197	2.1	0.0404	1.6	0.06537	1.2	0.83	804	13	799	12	800	13	786	24	102
	A20	79849	350	580	46	0.09	0.13500	1.9	1.221	2.1	0.0410	1.7	0.06556	0.9	0.90	817	15	810	12	811	13	792	19	103
	A21	62751	289	470	48	0.16	0.13290	2.0	1.205	2.2	0.0406	1.8	0.06575	0.9	0.90	804	15	803	12	805	14	798	20	101
	A22	68185	285	590	58	0.13	0.13320	3.3	1.207	3.4	0.0404	1.7	0.06573	1.1	0.95	806	25	804	19	800	13	798	22	101
	A23	77876	210	440	60	0.10	0.13290	7.5	1.203	7.6	0.0409	1.8	0.06566	1.0	0.99	804	57	802	43	810	14	796	20	101
	A24	34190	155	140	24	0.19	0.13390	1.7	1.213	2.2	0.0412	1.9	0.06569	1.4	0.76	810	13	806	12	816	15	796	30	102
	A25																							
	A26	59345	257	290	32	0.12	0.13320	2.1	1.208	2.3	0.0404	1.8	0.06577	0.9	0.92	806	16	804	13	801	14	799	19	101
	A27	63086	279	380	38	0.08	0.13120	2.1	1.187	2.4	0.0410	2.0	0.06562	1.0	0.90	795	16	795	13	813	16	794	22	100
Matongo (RGM 9672)	AS9672																							
	A28	9290	102	11	0.12	0.14	0.11470	1.7	0.988	2.7	0.0353	3.0	0.06248	2.1	0.62	700	11	698	14	702	21	691	45	101
	A33	17991	191	37	3.1	0.12	0.11910	1.6	1.039	2.3	0.0342	1.6	0.06327	1.7	0.69	725	11	723	12	679	11	717	36	101
	A34	34306	184	23	0.61	0.12	0.11510	1.9	0.9984	2.2	0.0351	2.2	0.0629	1.3	0.83	702	12	703	11	697	15	705	27	100
	A35	32867	92	12	1.0	0.07	0.11530	2.0	1.001	2.4	0.0349	2.1	0.06299	1.3	0.85	703	14	705	12	693	14	708	27	99
	A36	15794	5	1.7	7.8	0.07	0.11620	1.7	1.007	2.3	0.0351	2.2	0.06289	1.5	0.74	708	11	707	12	697	15	704	33	101
	A37	756	3	0.33	1.4	0.46	0.10720	2.3	0.933	6.2	0.0342	6	0.06314	5.7	0.37	656	14	669	31	680	38	713	122	92
	A38	839	5	0.68	0.96	3.98	0.11800	3.2	1.027	8.0	0.0342	5.5	0.06315	7.3	0.41	719	22	718	42	681	37	713	155	101
	A39	1161	370	40	0.01	1.25	0.11770	2.5	1.031	6.1	0.0348	5	0.06355	5.6	0.40	717	17	719	32	692	35	727	119	99
	A40	66658	33	25	23.6	0.07	0.11590	1.9	1.006	2.1	0.0353	1.7	0.06295	1.0	0.89	707	13	707	11	702	12	707	21	100
	A41	5876	640	68	0.06	0.26	0.11410	1.9	0.9977	3.1	0.0351	2.5	0.06342	2.5	0.61	696	13	703	16	698	17	722	52	96
	A42	113417	242	73	7.1	0.09	0.11600	2.0	1.009	2.1	0.0360	1.7	0.06309	0.9	0.91	708	13	708	11	714	12	711	19	99
	A43	40012	251	33	1.1	0.08	0.11520	1.7	0.9983	2.0	0.0348	2.0	0.06285	1.1	0.84	703	11	703	10	691	14	703	23	100
	A44	41164	645	81	0.8	0.09	0.11320	1.6	0.984	2.0	0.0352	1.6	0.06307	1.1	0.82	691	11	696	10	700	11	711	24	97
	A45	112129	293	83	6.5	0.06	0.11500	2.0	0.998	2.2	0.0346	1.8	0.06295	0.8	0.93	702	14	703	11	687	12	707	17	99
	A46	57579	117	27	4.6	1.56	0.11450	1.9	0.9935	3.9	0.0349	1.9	0.06294	3.4	0.49	699	13	701	20	693	13	706	73	99
	A47	19585	158	21	1.0	0.14	0.11650	1.9	1.008	2.4	0.0356	1.8	0.06274	1.5	0.79	710	12	708	12	707	13	699	31	102
	A48	27067	224	32	1.3	0.14	0.11690	1.8	1.013	2.2	0.0349	1.8	0.06286	1.3	0.81	713	12	710	11	694	12	704	28	101
	A49	36540	471	57	0.6	0.04	0.11440	2.0	0.9951	2.2	0.0361	1.9	0.06307	1.1	0.88	698	13	701	11	717	13	711	22	98
	Plesovice[g]	63692	629	32	0.14	0.10	0.05328	1.7	0.3866	2.0	0.0169	3.6	0.05263	1.0	0.87	335	6	332	6	339	12	313	22	107
	Plesovice	61546	640	33	0.13	0.23	0.05403	1.7	0.3954	2.0	0.0166	3.3	0.05307	1.2	0.81	339	5	338	6	332	11	332	27	102
	Plesovice	58128	636	32	0.15	0.12	0.05370	1.8	0.3905	2.1	0.0168	3.0	0.05273	1.1	0.84	337	6	335	6	336	10	317	26	106

IRP[g]	76402	174	16	1.3	14.51	0.05646	2.9	0.4198	6.9	0.0175	10.3	0.05393	6.3	0.42	354	10	356	21	350	36	368	142	96
IRP	80599	153	14	0.8	18.29	0.05741	2.8	0.4281	7.3	0.0180	6.5	0.05409	6.7	0.38	360	10	362	22	361	23	375	152	96

Spot size = 28 μm; depth of crater ~20 μm. $^{206}Pb/^{238}U$ error is the quadratic additions of the within run precision (2 SE) and the external reproducibility (2 SD) of the reference zircon. $^{207}Pb/^{206}Pb$ error propagation (^{207}Pb signal dependent) following Gerdes and Zeh (2009). $^{207}Pb/^{235}U$ error is the quadratic addition of the $^{207}Pb/^{206}Pb$ and $^{206}Pb/^{238}U$ uncertainty.

[a] Within run background-corrected mean ^{207}Pb signal in cps (counts per second).

[b] U and Pb content and Th/U ratio were calculated relative to GJ-1 reference zircon.

[c] Percentage of the common Pb on the ^{206}Pb. b.d. = below dectection limit.

[d] Corrected for background, within-run Pb/U fractionation (in case of $^{206}Pb/^{238}U$) and common Pb using model Pb composition and subsequently normalised to GJ-1 (ID-TIMS value/measured value); $^{207}Pb/^{235}U$ calculated using $^{207}Pb/^{206}Pb/(^{238}U/^{206}Pb * 1/137.88)$.

[e] rho is the $^{206}Pb/^{238}U/^{207}Pb/^{235}U$ error correlation coefficient.

[f] Degree of concordance = $^{206}Pb/^{238}U$ age/$^{207}Pb/^{206}Pb$ age × 100.

[g] Accuracy and reproducibilty was checked by analyses of Plesovice zircon and Ice River perovskite.

we have obtained (705.5 ± 4.5 Ma) provides a robust age of the carbonatite emplacement and rapid cooling. Regarding the discrepancy of 30–40 Ma between this age and older ages obtained on the Massif with other techniques, two explanations are suggested: (1) although unlikely because of the size of the URAPC, the possibility of a long time span between the main magmatic building stage of the intrusion and the latest stages of hydrothermal activity around the central Matongo carbonatite remains and (2) previous ages in the range 735–750 were not as accurate as the new La–ICP–MS age obtained in this study. New geochronological work on the magmatic facies would help to constrain this hypothesis.

For Lueshe, regardless of the exact origin of the zircon megacrysts (magmatic vs. hydrothermal), the age obtained here is significantly different from the La–ICP–MS age of the Matongo megacrysts and also from the ages around 735–750 Ma for the URAPC. Therefore, the crystallization age of the Lueshe zircon dates the emplacement of the Lueshe intrusion at ca. 800 Ma, significantly older than the age of the URAPC-Matongo emplacement.

7.3.2. Structural reactivation of the present-day region of the Western Rift and relation to Rodinia breakup

As suggested by several authors (Burke et al., 2003; Hanson, 2003; Kampunzu et al., 1997, 1998; Tack et al., 1984, 1996), most of the Proterozoic ages obtained for the 23 envisaged alkaline complexes and/or carbonatites along the present-day Western Rift seem to reflect uprise of mantle-derived magmas along lithospheric weakness zones in relation with the breakup of Rodinia (Fig. 9). This breakup is recorded at ca. 705 Ma at Matongo by the La–ICP–MS age of the zircon megacrysts and at ca. 798 Ma at Lueshe by the same method.

In addition to alkaline magmatism, Neoproterozoic reactivation of older structures is also illustrated by the formation of intracratonic basins (Fernandez-Alonso et al., 2012; Tack et al., 1992): (1) the Malagarazi basin located across the Burundi Tanzania border (Fig. 1B). CFB-type rocks (“Kabuye-Gagwe amygdaloidal basalts”), intercalated in the sedimentary succession of the Neoproterozoic Malagarazi–Nyamuri (formerly Bukoba) Supergroup, yielded a crystallization age of 795 ± 7 Ma (Deblond et al., 2001); and (2) the Itombwe syncline (DRC, Fig. 1B), This narrow N–S elongated structure contains a sedimentary succession (Neoproterozoic Itombwe Supergroup), with a maximum deposition age of ~710 Ma (Fernandez-Alonso et al., 2012; Villeneuve, 1987; Walemba and Master, 2005).

The considered ~700–800 Ma time-period tracing both endogenic and exogenic extensional processes thus records diachronous reactivation and breakup of Rodinia supercontinent in response to differential intraplate stress, in agreement with geodynamic processes invoked by Li et al. (2008), Eyles and Januszczak (2004) and Eyles (2008). In the nearby Congo Craton and at its margin, the diacronicity of the breakup and the succession of extensional regimes have been evidenced in the time frame ~1 Ga to ~500 Ma by the formation of sedimentary basins (e.g. Delpomdor et al., 2013) and alkaline magmatism (e.g. Pedrosa-Soares and Flecha de Alkmim, 2011).

However, the configuration, evolution and even existence of the Rodinia supercontinent remain debated. Even though most of the autors consider that the supercontinent fragmentation and dipersal began about 800–750 Ma (Hoffman, 1999; Pisarevsky et al., 2003) or even 1 Ga ago (Eyles, 2008), others argued that (1) Rodinia breakup occurred between 750 and 600 Ma (Eyles and Januszczak, 2004; Li et al., 2008) or even not before 725 Ma (Powell et al., 1993) and (2) the formation of Gondwana by the reassemblage of the dispersed terranes ended at about 550 Ma (Meert and Van der Voo, 1997). It has also been proposed that the early Panafrican tectonic phase began around 725 Ma (Lenoir et al., 1994). In this context,

Table 6
Sr and Nd isotopic data of samples from the Matongo carbonatites (Demaiffe, 2008).

Sample	Description	$^{87}Rb/^{86}Rb$	$^{87}Sr/^{86}Sr(i)$	$^{147}Sm/^{144}Nd$	$^{143}Nd/^{144}Nd$	$^{143}Nd/^{144}Nd(i)$	εNd(i)
Matongo carbonatite (Demaiffe, 2008)							
Gi3-ITS4/84-87m	Sövite II	0.0016	0.70314	0.0784	0.512273	0.511913	5.2
Gi2-S3/147	Sövite II	0.0134	0.70311	0.0802	0.512233	0.511865	3.1
Gi12-S5/121.5m	Sövite II with apatite	0.0001	0.70306	#N.A.	#N.A.	#N.A.	#N.A.
Gi1-S2/171-172m	Sövite II with apatite and px	0.0071	0.70294	0.0725	0.512273	0.511940	4.6
Gi10-S6/155-156m	Sövite II with apatite and px	0.0024	0.70357	#N.A.	#N.A.	#N.A.	#N.A.
Gi11-S8/56m	px and apatite cumulate	0.0061	0.70344	0.0733	0.512052	0.511716	0.2
Gi16-S3/121m	Ferrocarbonatite	0.0066	0.70321	0.0790	0.512205	0.511843	2.7
Gi17-S7/91-95	"Late" hydrothermal carbonatite	0.0268	0.71425	0.8398	0.513487	0.509634	-44.0
Gi5-ITS3/291	kfs-fenite	0.4031	0.70280	#N.A.	#N.A.	#N.A.	#N.A.
Gi14-ITS4/150	kfs-fenite	0.0938	0.70350	#N.A.	#N.A.	#N.A.	#N.A.
Gi15-S5/104-106	bt-fenite	0.2747	0.70400	0.0932	0.512303	0.511875	3.3

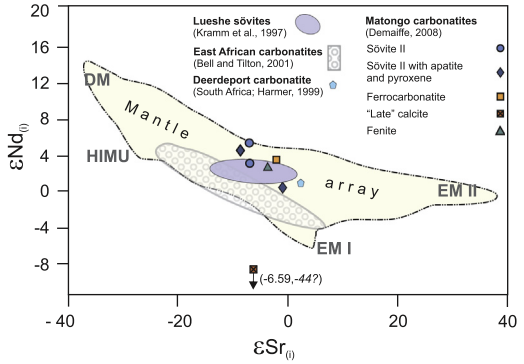

Fig. 8. Initial εNd–εSr isotopic diagrams for the various Matongo carbonatites (7 samples; Demaiffe, 2008). For comparison, are reported the fields for the sövites from the Lueshe Neoproterozoic carbonatite (DRCongo; Kramm et al., 1997) and for the East African carbonatites (dated between 200 and 0 Ma; Bell and Tilton, 2001). The positions of the main oceanic mantle reservoirs identified by Zindler and Hart (1986) are shown: DM = depleted mantle, BSE = bulk silicate earth, EMI and EMII = enriched mantle I and II, HIMU = high U/Pb domain. Outline of the mantle array (dashed line) is drawn after Stracke et al. (2003) and Bizimis et al. (2003).

the emplacement of late mylonitic granites along shear zones at 724 ± 6 Ma (U–Pb age on zircon fraction) in the Ubendian belt of SW Tanzania could be the result of a continental collision in the frame of the early Panafrican orogen (Theunissen et al., 1992). On a larger scale, Fritz et al. (2013) have proposed that the consolidation of the East African orogen was achieved during distinct phases between ~850 and 550 Ma, with the accretion of microcontinents during the ~850–620 Ma time range. The abundance of granitoid magmatism occurring between ~850 and ~650 Ma in the East Africa domain may be related to this continental aggregation leading to the formation of the Gondwana supercontinent (Kröner and Cordani, 2003). If an extensional tectonic setting is considered for that period, what remains debated, the URAPC would represent one of the last episodes of the magmatic activity associated with this event, before the "renewal" of alkaline/carbonatitic activity in the area several hundred millions years later during the Cretaceous (e.g. Chilwa in Malawi; Simonetti and Bell, 1994), in relation with the develoment of the East African rift system.

7.3.3. Early continental rifting in the Rodinia breakup history: the involvement of a plume?

Many alkaline complexes of Central Africa were emplaced between ~750 and 650 Ma. However, some complexes record significantly older ages, in the range ~830–750 Ma, among which the now dated Lueshe complex, of which the zircon megacrysts have been dated at 798.5 ± 4.9 Ma. These old emplacement could also be related to the Rodinia breakup, especially to an earlier step of intraplate continental rifting. This could possibly be associated with the presence of a superplume below Rodinia (Li et al., 2008) that eventually led to the breakup of the supercontinent. In the western branch of the East African Rift, the presence of flood basalts spatially and temporally associated with the alkaline complexes favours the involvement of a superplume (Bell, 2001; Ernst and Buchan, 2003). Tholeiitic fissural flood basalts, like the Kabuye–Gagwe amygdoidal lavas, emplaced in the Malagaraszi basin (De Paepe et al., 1991) at 822 ± 30 Ma (K–Ar ages; Briden et al., 1971 in Deblond et al., 2001; Fig. 9) and between 815 ± 14 and 709 ± 2 Ma (Ar–Ar ages; Deblond et al., 2001; Fig. 9). They are also coeval with the shallow-depth Nyaganza dolerites that are intrusive in the Malgarasian Subgroup (815 ± 14 Ma; K–Ar age; Cahen et al., 1984) and with the doleritic gabbros of Kavumwe, dated at 803 ± 30 Ma, 806 ± 30 Ma (K-Ar method; Briden et al., 1971) and 795 ± 7 Ma (Deblond et al., 2001). However, additional arguments should be found for a proper demonstration of a mantle plume involvement in the URAPC genesis; this hypothesis would be especially challenging if a convergent plate tectonic setting (Panafrican orogeny) is favoured in the future rather than an extensional setting (Rodinia Breakup).

7.3.4. Panafrican overprint

In the present-day Western Rift region, discrete Panafrican tectonic overprint with a climax at ~550 Ma is considered a far-field effect of the distant East African Orogen facilitated by the palaeogeography of the Archean Tanzania Craton, which plays as an indentor squeezing the Proterozoic rocks (De Waele et al., 2008; Fernandez-Alonso et al., 2012; Dewaele et al., 2011). Due to the easy diffusion of radiogenic ^{87}Sr and ^{40}Ar and the high mobility of K, Rb and Sr, this Panafrican overprint resulted in disturbance and partial resetting of the K–Ar, Ar–Ar and Rb–Sr isotopic systems with a huge scatter of apparent ages as documented in Fig. 9, explaining some if not most of the younger 580–450 Ma ages for several alkaline complexes (Fig. 9). It is particularly obvious for the Kirumba complex (RDC), where the Rb–Sr and K–Ar ages are situated between 800 and 240 Ma (Bellon and Pouclet, 1980; Cahen et al., 1979; Cahen and Snelling, 1966; Kampunzu et al., 1998). This could also be the case for Lueshe, where most of the previously obtained ages (see Geological context) are significantly younger than the new LA–ICP–MS age on zircon megacrysts (798.5 ± 4.9 Ma). This may not be the case for the URAPC for which the U–Pb age on zircon megacryst at 705 Ma is indinstiguishable from the Rb-Sr whole rocks age (699 Ma).

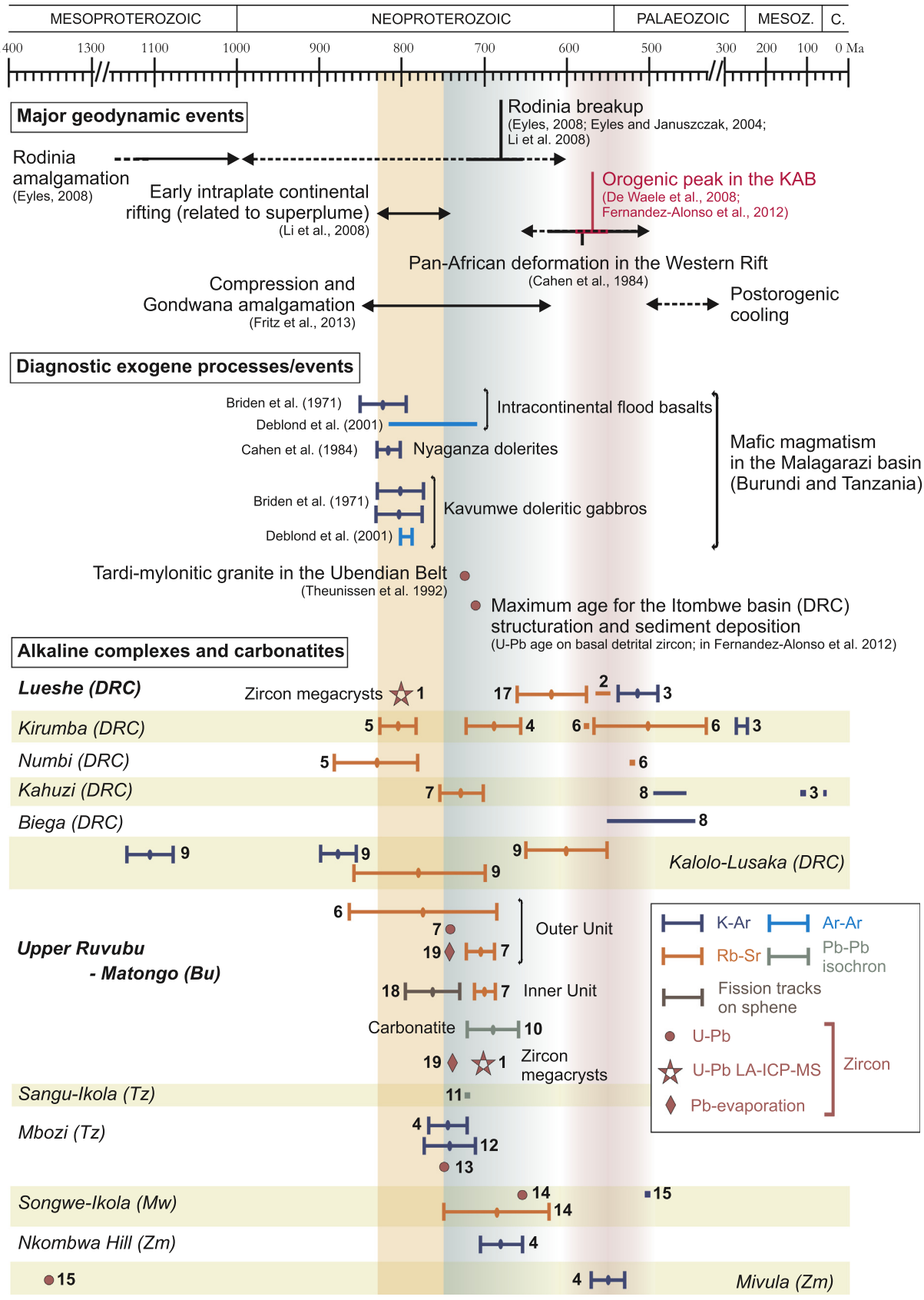

Fig. 9. Schematic diagram comparing the isotopic ages obtained on carbonatites and alkaline complexes (located in Fig. 1B) and the new Matongo and Lueshe zircon U–Pb ages. All these ages are considered together and reinterpreted in the regional geodynamic context. Reference numbering is as follow: (1) This paper; (2) Kramm et al., 1997; (3) Bellon and Pouclet, 1980; (4) Cahen and Snelling, 1966; (5) Kampunzu et al., 1998; (6) Cahen et al., 1979; (7) Tack et al., 1984; (8) Vellutini et al., 1981; (9) Cahen et al., 1975; (10) Demaiffe, 2008; (11) Stendal et al., 2004; (12) Brock, 1968; (13) Mbede et al., 2004; (14) Ray, 1974; (15) Snelling et al., 1964; (16) Vrana et al., 2004; (17) Van Overbeke, 1996; (18) Van den Haute, 1986; (19) Tack et al., 1995.

8. Conclusion

Petrographic observation and geochemical data (major and trace element analyses) show that different magmatic processes occurred at the scale of the Matongo carbonatite: fractionation of clinopyroxene (and apatite) during carbonatite emplacement, ankeritisation, and alkali loss inducing fenitisation. "Late" hydrothermal processes developed after carbonatite emplacement and affected the primary facies of the carbonatite.

In the hypothesis of an extensional setting, the ~800 and ~705 Ma ages obtained on carbonatite-related zircon crystals from Lueshe (DRC) and Matongo (Burundi) could confirm the relationship between carbonatite emplacement and Rodinia breakup, either during an early stage of the fragmentation (at ~800 Ma, for the Lueshe complex) or at a later stage (at ~705 Ma for the Matongo carbonatite). The ages of the alkaline complexes would also illustrate the reactivation of Palaeoproterozoic lithospheric weakness zones during extension. Other expressions of the continental rifting process at that time could be found in the formation of Neoproterozoic intracratonic basins documented in the KAB (Fernandez-Alonso et al., 2012; Tack et al., 1992). Consequently, the major lithospheric weaknesses remain the "key factor" controlling the emplacement/location of the carbonatites and alkaline complexes in the East African Rift system.

The Panafrican event (660–550 Ma) induced deformation in the KAB, which could be responsible for the disturbance and partial resetting of some isotopic systems. In the area of the western branch of the East African rift, the URAPC could correspond to one of the last episodes of the magmatic activity associated with Rodinia breakup, before the "renewal" of alkaline/carbonatitic activity during the Cretaceous in Central Africa.

Acknowledgments

This study is a contribution to the GECO project, funded by the Belgian Federal Public Service for Foreign Affairs. Andy Moore and Stefano Salvi are warmly thanked for their helpful comments that contributed to a nice amelioration of this paper. The authors are also grateful to Jean-Paul Liégeois for his constructive comments and editorial handling of the paper.

Appendix A. Supplementary material

Supplementary data associated with this article can be found, in the online version, at http://dx.doi.org/10.1016/j.jafrearsci.2014.08.010.

References

Bau, M., 1996. Controls on the fractionation of isovalent trace elements in magmatic and aqueous systems: evidence from Y/Ho, Zr/Hf, and lanthanide tetrad effect. Contrib. Miner. Petrol. 123, 323–333.

Bell, K., Simonetti, A., 1996. Carbonatite magmatism and plume activity: implications from the Nd, Pb and Sr isotope systematics of Oldoinyo Lengai. J. Petrol. 37, 1321–1339.

Bell K. 2001. Carbonatites: relationships tomantle-plume activity, in: Ernst, R.E., Buchan, K.L. (Eds.), Mantle Plumes: Their Identification Through Time, GSA Am. Spec. Pap. 352, pp. 267–90.

Bell, K., Tilton, G.R., 2001. Nd, Pb and Sr isotopic compositions of east African carbonatites: evidence for mantle mixing and plume inhomogeneity. J. Petrol. 42, 1927–1945.

Bellon, H., Pouclet, A., 1980. Datations K–Ar de quelques laves du rift-ouest de l'Afrique centrale; implication sur l'évolution magmatique et structurale. Geol. Rundsch. 69, 49–62.

Bizimis, M., Salters, V.M.J., Dawson, J.B., 2003. The brevity of carbonatite sources in the mantle: evidence from Hf isotopes. Contrib. Miner. Petrol. 145, 281–300.

Briden, J.C., Piper, J.D., Henthorn, D.I., Rex, D.C., 1971. New palaeomagnetic results from Africa and related potassium–argon age determinations. In: 15th Annual Report Research Institute African Geology, University of Leeds, pp. 46–50.

Brinckmann, J., Lehmann, B., 1983. Exploration de la bastnaésite-moncite dans la région de Gakara, Burundi. Rapport sur la phase I. Unpublished report, Bujumbura/Hannover, 157 p.

Brinckmann, J., Lehmann, B., Hein, U., Höhndorf, A., Mussallam, K., Weiser, T., Timm, F., 2001. La Géologie et la minéralisation primaire de l'or De La Chaîne Kibarienne, Nord-Ouest Du Burundi, Afrique Orientale. Geologisches Jahrbuch Reihe D : Heft 101, 195 p.

Brock, P., 1968. Metasomatic and intrusive nepheline-bearing rocks from the Mbozi syenite-gabbro complex, southwestern Tanzania. Can. J. Earth Sci. 5, 387–419.

Burke, E.A.J., 1998. New data on zircon from Matongo (Burundi). Aardk. Mededel. 8, 1–4.

Burke, K., Ashwal, L.D., Webb, S.J., 2003. New way to map old sutures using deformed alkaline rocks and carbonatites. Geology 31, 391–394.

Buysschaert, X., 1993. Mineralogisch en geochemisch onderzoek van de buitenste eenheid van het Alkalisch Plutonisch Complex van de Boven-Ruvubu (Burundi). Unpublished Master thesis University of Ghent, 121 p.

Cahen, L., Snelling, N., 1966. The Geochronology of Equatorial Africa. North-Holland Publishing Cy, Amsterdam, 195 p.

Cahen, L., Ledent, D., Snelling, N., 1975. Données géochronologiques dans le Katangien inférieur du Kasaï oriental et du Shaba nord-oriental (République du Zaïre). Rapport annuel 1974 du Département de Géologie et Minéralogie, Musée royal de l'Afrique centrale, Tervuren, pp. 59–70.

Cahen, L., Ledent, D., 1979. Précision sur l'âge, la pétrogenèse et la position stratigraphique des «granites à étain» dans l'est de l'Afrique centrale. Bull. Soc. belge de Géol. 88, 33–39.

Cahen, L., Ledent, D., Villeneuve, M., 1979. Existence d'une chaîne plissée protérozoique supérieur au Kivu oriental (Zaïre). Données géochronologiques relatives au Supergroupe de l'Itombwe. Bull. Soc. belge de Géol. 88, 71–83.

Cahen, L., Snelling, N.J., Delhal, J., Vail, J.R., Bonhomme, M., Ledent, D., 1984. The Geochronology and Evolution of Africa. Clarendon Press Oxford, 512 p.

Caruba, R., Iacconi, P., 1983. Les zircons des pegmatites de Narssârssuk (Groënland). L'eau et les groupements OH dans les zircons métamictes. Chem. Geol. 38, 75–92.

Chakhmouradian, A.R., 2006. High-field-strength elements in carbonatitic rocks: geochemistry, crystal chemistry and significance for constraining the sources of carbonatites. Chem. Geol. 235, 138–160.

De Paepe, P., Tack, L., Moens, L., Van de Velde, P., 1991. The basic magmatism of the Upper Proterozoic in South-East Burundi. Rapport annuel 1989–1990 du Département de Géologie et Minéralogie, Musée royal de l'Afrique central, Tervuren (Belgique), pp. 85–104.

De Waele, B., Johnson, S.P., Pisarevsky, 2008. Palaeoproterozoic to Neoproterozoic growth and evolution of the eastern Congo Craton: Its role in the Rodinia puzzle. Precambrian Research 160, 127–141.

Deblond, A., Punzalan, L.E., Boven, A., Tack, L., 2001. The Malagarazi Supergroup of SE Burundi and its correlative Bukoban Supergroup of NW Tanzania: Neo – and Mesoproterozoic chronostratigraphic constraints from Ar–Ar ages on mafic intrusive rocks. J. Afr. Earth Sc. 32, 435–449.

Delpomdor, F., Linnemann, U., Boven, A., Gärtner, A., Travin, A., Blanpied, C., Virgone, A., Jelsma, H., Préat, A., 2013. Depositional age, provenance, and tectonic and paleaclimatic settings of the late Mesoproterozoic-middle Neoproterozoic Mbuji-Mayi Supergroup, Democratic Republic of Congo. Palaeogeogr. Palaeoclimatol. Palaeoecol. 389, 4–34.

Demaiffe, D., 2008. Le magmatisme alcalin et carbonatitique: synthèse sur la province paléozoïque de Kola (Russie) et caractéristiques générales du massif protérozoïque de Matongo (Burundi). Bull. Séances de l'Acad. Roy. Sci. d'Outre-Mer 54, 171–196.

Dewaele, S., Henjes-Kunst, F., Melcher, F., Sitnikova, M., Burgess, R., Gerdes, A., Fernandez, M.A., De Clerq, F., Muchez, P., Lehmann, B., 2011. Late Neoproterozoic overprinting of the cassiterite and columbite-tantalite bearing pegmatites of the Gatumba area, Rwanda (Central Africa). J. Afr. Earth Sc. 61, 10–26.

Ernst, R.E., Buchan, K.L., 2003. Recognizing mantle plumes in the geological record. Annu. Rev. Earth Planet. Sci. 31, 469–523.

Eyles, N., 2008. Glacio-epochs and the supercontinent cycle after ~3.0 Ga: tectonic boundary conditions for glaciation. Palaeogeogr. Palaeoclimatol. Palaeoecol. 258, 89–129.

Eyles, N., Januszczak, N., 2004. 'Zipper-rift': a tectonic model for the Neoproterozoic glaciations during the breakup of Rodinia after 750 Ma. Earth Sci. Rev. 65, 1–73.

Fernandez-Alonso, M., Cutten, H., De Waele, B., Tack, L., Tahon, A., Baudet, D., Barritt, S.D., 2012. The Mesoproterozoic Karagwe-Ankole Belt (formerly the NE Kibara Belt): the result of prolonged extensional intracratonic basin development punctuated by two short-lived far-field compressional events. Precambr. Res. 216, 63–86.

Fransolet, A.M., Tack, L., 1992. Les zircons de Matongo (Burundi) et leur signification. Ann. Soc. géol. de Belgique 115, 113–118.

Fritz, H., Abdelsalam, M., Ali, K.A., Bingen, B., Collins, A.S., Fowler, A.R., Ghebread, W., Hauzenberger, C.A., Johnson, P.R., Kusky, T.M., Macey, P., Muhongo, S., Stem, R.J., Viola, G., 2013. Orogen styles in the East African Orogen: a review of the Neoproterozoic to Cambrian tectonic evolution. J. Afr. Earth Sci. 86, 65–106.

Gerdes, A., Zeh, A., 2006. Combined U–Pb and Hf isotope LA–(MC–)ICP–MS analyses of detrital zircons: comparison with SHRIMP and new constraints for the provenance and age of an Armorican metasediment in Central Germany. Earth Planet. Sci. Lett. 249, 47–61.

Gerdes, A., Zeh, A., 2009. Zircon formation versus zircon alteration – new insights from combined U–Pb and Lu–Hf in-situ LA–ICP–MS analyses, and consequences for the interpretation of Archean zircon from the Limpopo Belt. Chem. Geol. 261, 230–243.

Hanson, R.E., 2003. Proterozoic geochronology and tectonic evolution of southern Africa. In: Yoshida, M., et al. (Eds.), Proterozoic East Gondwana: Supercontinent assembly and breakup, Geological Society, London, Special Publications, 206, pp. 427–463.
Hoffman, P.F., 1999. The break-up of Rodinia, birth of Gondwana, true polar wander and the snowball Earth. J. Afr. Earth Sc. 28, 17–33.
Hoskin, P.W.O., Schaltegger, U., 2003. The Composition of Zircon and Igneous and Metamorphic Petrogenesis. Rev. Mineral. Geochem. 53, 27–62.
Kalt, A., Hegner, E., Satir, M., 1997. Nd, Sr, and Pb isotopic evidence for diverse lithospheric mantle sources of East African Rift carbonatites. Tectonophysics 278, 31–45.
Kampunzu, A.B., Lubala, R.T., Makutu, M.N., Caron, J.P.H., Rocci, G., Vellutini, P.J., 1985. Alkaline complexes from the interlake region of eastern Zaire and Burundi – an example of anorogenic massifs in the relaxation stage. J. Afr. Earth Sc. 3, 151–167.
Kampunzu, A.B., Kramers, J., Tembo, F., 1997. Neoproterozoic alkaline and carbonatite magmatism along the western rift in Central-Eastern Africa: break-up of Rodinia supercontinent and reconstruction of Gondwana. Gondwana Res. 1, 155–156.
Kampunzu, A.B., Kramers, J.D., Makutu, M.N., 1998. Rb–Sr whole rock ages of the Lueshe, Kirumba and Numbi igneous complexes (Kivu, Democratic Republic of Congo) and the break-up of the Rodinia supercontinent. J. Afr. Earth Sc. 26, 29–36.
Kampunzu, A.B., Mohr, P., 1991. Magmatic evolution and petrogenesis in the east African Rift System. In: Kampunzu, A.B., Lubala, R.T. (Eds.), Magmatism in Extensional Structural Settings: The Phanerozoic African plate. Springer-Verlag, Berlin, pp. 85–136.
Kontak, D.J., Clark, A.H., 2002. Genesis of the giant, bonanza San Rafael Lode tin deposit, Peru: origin and significance of pervasive alteration. Econ. Geol. 97, 1741–1777.
Kramm, U., Maravic, H.v., Morteani, G., 1997. Neodynium and Sr isotopic constraints on the petrogenetic relationships between carbonatites and cancrinite syenites from the Lueshe Alkaline Complex, east Zaire. J. Afr. Earth Sci. 25, 55–76.
Kröner, A., Cordani, U., 2003. African, southern Indian and South American cratons were not part of the Rodinia supercontinent: evidence from field relationships and geochronology. Tectonophysics 375, 325–352.
Le Bas, M.J., 1981. Carbonatite magmas. Mineral. Mag. 44, 133–140.
Le Bas, M.J., 1984. Nephelinites and carbonatites. In: Fitton, J.G., Upton, B.G.J. (Eds.), Alkaline Igneous Rocks, The Geological Society of London, Special Publication, vol. 30, pp. 53–83.
Le Maitre, R.W., 2002. A classification of igneous rocks and glossary of terms. Cambridge Univerity Press, 236 p.
Lehmann, B., Nakai, S., Höhndorf, A., Brinckmann, J., Dulski, P., Hein, U., Masuda, A., 1994. REE mineralization at Gakara, Burundi: evidence for anomalous upper mantle in the western Rift Valley. Geochim. Cosmochim. Acta 58, 985–992.
Lenoir, J.L., Liégeois, J.P., Theunissen, K., Klerkx, J., 1994. The Palaeoproterozoic Ubendian shear belt in Tanzania: geochronology and structure. J. Afr. Earth Sc. 19, 169–184.
Li, Z.X., Bogdanova, S.V., Collins, A.S., Davidson, A., De Waele, B., Ernst, R.E., Fitzsimons, I.C.W., Fuck, R.A., Gladkochub, D.P., Jacobs, J., Karlstrom, K.E., Lu, S., Natapov, L.M., Pease, V., Pisarevsky, S.A., Thrane, K., Vernikovsky, V., 2008. Assembly, configuration, and break-up history of Rodinia: a synthesis. Precambr. Res. 160, 179–210.
Maravic, H.v., 1983. Geochemische und petrographische Untersuchungen zur Genese des niobführenden Karbonatit/Cancrcinit-Syenitkomplexes von Lueshe, Kivu. NE Zaïre. Unpublished PhD thesis, Technische Universität Berlin, 330 p.
Maravic, H.v., Morteani, G., 1980. Petrology and geochemistry of the carbonatite and syenite complex of Lueshe (NE Zaire). Lithos 13, 159–170.
Maravic, H.v., Morteani, G., Roethe, G., 1989. The cancrinite-syenite/carbonatite complex of Lueshe, Kivu/NE-Zaire: petrographic and geochemical studies and its economic significance. J. Afr. Earth Sci. 9, 341–355.
Mbede, E.I., Kampunzu, A.B., Armstrong, R.A., 2004. Neoproterozoic inheritance during Cainozoic riting in the western and southwestern branches of the East African Rift system: evidence from carbonatites and alkaline intrusions. In: International conference "The East African Rift system: Geodynamics, resources, and environment, June 20–24 2004, Addis Ababa (Ethiopia). Abstract book, p. 142.
McDonough, W.F., 1990. Constraints on the composition of the continental lithospheric mantle. Earth Planet. Sci. Lett. 101, 1–18.
McDonough, W.F., Sun, S.S., Ringwood, A.E., Jagoutz, E., Hofmann, A.W., 1992. Potassium, Rubidium and Cesium in the Earth and Moon and the evolution of the mantle of the Earth. Geochim. Cosmochim. Acta 56, 1001–1012.
Meert, J.G., Van der Voo, R., 1997. The assembly of Gondwana 800–550 Ma. J. Geodyn. 23, 223–235.
Melcher, F., Graupner, T., Gäbler, H.E., Sitnikova, M., Henjes-Kunst, F., Oberthür, T., Gerded, A., Dewaele, S., 2013. Tantalum-(niobium-tin) mineralisation in African pegmatites and rare metal granites: Constraints from Ta-Nb oxide mineralogy, geochemistry and U-Pb geochronology. Ore Geol. Rev., in press.
Midende, G., 1984. La carbonatite de Matongo (Burundi). Unpublished PhD thesis, Université Libre de Bruxelles, Bruxelles, 288 p.
Philippo, S., 1995. Evaluation minéralogique par diffraction des rayons X qualitative et quantitative des gisements latéritiques de niobium de la Lueshe et de Bingo dans le cadre de l'optimisation de la récupération du pyrochlore. Unpublished PhD thesis. Université Catholique de Louvain, Belgium, 207p.
Pisarevsky, S.A., Wingate, M.T.D., Powell, C.McA., Johnson, S.P., Evans, D.A.D., 2003. Models of Rodinia assembly and fragmentation. In: Yoshida, M., Windley, B.F., Dasgupta, S. (Eds.), Proterozoic East Gondwana: Supercontinent Assembly and Break-up. Geological Society of London, Special Publication 206, pp. 35–55.
Pedrosa-Soares, A.C., de Alkmim, Flecha., 2011. How many rifting events preceded the development of the Araçuai-West Congo orogen? Geonomos 19, 244–251.
Powell, C.Mc.A., Li, Z.X., McElhinny, M.W., Meert, J.G., Park, J.K., 1993. Paleomagnetic constraints on timing of the Neoproterozoic break-up of Rodinia and the Cambrian formation of Gondwana. Geology 21, 889–892.
Ray, G., 1974. The structural and metamorphic geology of northern Malawi. J. Geol. Soc. London 130, 427–440.
Romer, R.L., Lehmann, B., 1995. U-Pb columbite-tantalite age of Neoproterozoic Ta–Nb mineralisation in Burundi. Econ. Geol. 90, 2303–2309.
Simonetti, A., Bell, K., 1994. Isotopic and geochemical investigation of the Chilwa Island carbonatite complex, Malawi: evidence for a depleted mantle source region, liquid immiscibility, and open-system behaviour. J. Petrol. 35, 1597–1621.
Snelling, N., Hamilton, E., Drysdall, A., Stillman, C., 1964. A review of age determinations from Northern Rhodesia. Econ. Geol. 59, 961–981.
Stendal, H., Frei, R., Muhongo, S., Rasmussen, T.M., Mnali, S., Petro, F., Temu, E.B., 2004. Gold potential of the Mpanda Mineral Field, SW Tanzania: evaluation based on geological, lead isotopic and aeromagnetic data. J. Afr. Earth Sc. 38, 437–447.
Stracke, A., Bizimis, M., Salters, V.J.M., 2003. Recycling oceanic crust: quantitative constraints. Geochem., Geophys., Geosyst. 4. http://dx.doi.org/10.1029/2001GC000223.
Sun, S.S., 1982. Chemical composition and origin of the Earth's primitive mantle. Geochim. Cosmochim. Acta 46, 179–192.
Tack, L., De Paepe, P., Deutsch, S., Liégeois, J.P., 1984. The alkaline plutonic complexof the Upper Ruvubu (Burundi): geology, age, isotopic geochemistry and implications for the regional geology of the Western rift. In: Klerkx, J., Michot, J. (Eds.), African Geology, pp. 91–114.
Tack., L., Sindayihebura, A., Cimpaye, D., 1992. The Nkoma (SE Burundi): an episodically reactivated Lower Burundian (Middle Proterozoic) siliciclastic sequence, locally overlain by a Malagarasian (Upper Proterozoic) sedimentary breccias. IGCP n 255 Newsletter 4, 31–43.
Tack, L., Liégeois, J.P., André, L., Navez, J., 1995. The Upper Ruvubu alkaline plutonic complex (Burundi). Annual Report of the Royal Museum for Central Africa, Tervuren, p. 9.
Tack, L., Deblond, A., De Paepe, P., Duchesne, J.C., Liégeois, J.P., 1996. Proterozoic alignements of alkaline plutons revealing lithospheric discontinuities : evidence from Eastern Africa, in: Demaiffe, D. (Ed.), Petrology and Geochemistry of magmatic suites of rocks in the continental and oceanic crusts. A volume dedicated to Professor Jean Michot, Université Libre de Bruxelles, Bruxelles, Belgium, pp. 219–226.
Tack, L., Wingate, M.T.D., De Waele, B., Meert, J., Belousova, E., Griffin, A., Tahon, A., Fernandez-Alonso, M., 2010. The 1375 Ma "Kibaran event" in Central Africa: prominent emplacement of bimodal magmatism under extensional regime. Precambr. Res. 180, 63–84.
Theunissen, K., Lenoir, J.L., Liégeois, J.P., Delvaus, D., Mruma, A., 1992. Empreinte pan-africane majeure dans la chaîne ubendienne de Tanzanie sud-occidentale: géochronologie U–Pb sur zircon et contexte structural. Comptes Rendus de l'Académie des Sciences de Paris 314, 1355–1362.
Van den Haute, P., 1986. Sphene fission-track dating of a precambrian lakaline pluton in Burundi (Central Africa). Terra Cognita 6, 165.
Van Overbeke, A.C., 1996. Le complexe à carbonatite et syénite de la Lueshe (N-Kivu, Zaïre): pétrogenèse des roches ignées et caractérisation géochimique des processus métasomatiques (fénitisation). Unpublished PhD thesis. Université Catholique de Louvain, Louvain-la-Neuve, Belgique. 235 p.
Van Overbeke, A.C., Demaiffe, D., Verkaeren, J., 1996. The syenite-carbonatite complex of Lueshe (NE Zaire): petrography, geochemistry and Rb–Sr chronology. In Demaiffe, D. (Ed.), Petrology and Geochemistry of magmatic suites of rocks in the continental and oceanic crusts. A volume dedicated to Professor Jean Michot, Université Libre de Bruxelles, Bruxelles, Belgium, pp. 355–370.
Van Wambeke, L., 1977. The Karonge rare earth deposits, Republic of Burundi: new mineralogical and geochemical data and origin of the mineralization. Miner. Deposita 12, 373–380.
Vellutini, P., Bonhomme, C., Caron, M., Kampunzu, A.B., Lubala, T., 1981. Sur la signification tectonique des complexes alcalins acides de Kahuzi et de Biega (Kivu, Zaire). Comptes Rendus de l'Académie des Sciences de Paris 292, 1027–1029.
Vergauwen, I., 1990. Mineralogisch en geochemisch onderzoek van de nefeliensyenieten van het Alkalisch Plutonisch Complex van de Boven-Ruvubu (Burundi). Unpublished Master thesis University of Ghent, 80 p.
Verwoerd, 1967. The carbonatites of South Africa and South West Africa. Handbook 6 of the Geological Society of South Africa, 452 p.
Villeneuve, M., 1987. Géologie du synclinal de l'Itombwe (Zaïre oriental) et le problème de l'existence d'un sillon plissé pan-africain. J. Afr. Earth Sc. 6, 869–880.
Vrana, S., Kachlik, V., Kroner, A., Marheine, D., Seifert, A.V., Zacek, V., Baburek, J., 2004. Ubendian basement and its late Mesoproterozoic and early Neoproterozoic structural and metamorphic overprint in northeastern Zambia. J. Afr. Earth Sc. 38, 1–21.

Walemba, K., Master, S., 2005. Neoproterozoic diamictites from the Itombwe Synclinorium, Kivu Province, Democratic Republic of Congo: palaeoclimatic significance and regional correlations. J. Afr. Earth Sc. 42, 200–210.
Woolley, A.R., 2001. Alkaline rocks and carbonatites of the world. Part 3: Africa, Geological Society of London, 372 p.
Zeh, A., Gerdes, A., 2012. U–Pb and Hf isotope record of detrital zircons from gold-bearing sediments of the Pietersburg Greenstone Belt (South Africa) – is there a common provenance with the Witwatersrand Basin? Precambr. Res. 204–205, 46–56.
Zhao, Z.-F., Zheng, Y.-F., Wei, C.-S., Gong, B., 2004. Temporal relationship between granite cooling and hydrothermal uranium mineralization at Dalongshan in China: a combined radiometric and oxygen isotopic study. Ore Geol. Rev. 25, 221–236.
Zindler, A., Hart, S., 1986. Chemical geodynamics. Annu. Rev. Earth Planet. Sci. 14, 493–571.